Cambridge Centre for Computational Chemical Engineering

University of Cambridge

Department of Chemical Engineering

A New Model for the Drying of Droplets Containing Suspended Solids after Shell Formation

Christopher Handscomb [1]   Markus Kraft [1]   Andrew Bayly [2]

released: 23 June 2008

[1] Department of Chemical Engineering
University of Cambridge
Pembroke Street
Cambridge CB2 3RA
UK
E-mail: mk306@cam.ac.uk

[2] Procter and Gamble
Newcastle Technical Centre
Whitley Road
Longbenton
Newcastle NE12 9TS
UK
E-mail: bayly.ae@pg.com

c4e

Abstract

The novel droplet drying model introduced by the authors in a previous paper is extended to droplets drying in the presence of a surface shell. The model now incorporates shell thickening, along with a description of wet and dry shell drying. Structural properties of the shell are included in the model and influence the predicted dried particle morphology. Comparisons between model predictions and experimental data from the literature are presented for two systems of interest: detergent crutcher mix and colloidal silica. These simulations demonstrate the model is capable of predicting dried particle morphology together with other properties of interest such as moisture profiles and moments of the solids particle size distribution.

1

Contents

1 Introduction

Spray drying is the operation of choice for the production of many commercial products ranging from high value pharmaceuticals to bulk commodities such as dried milk, [35]. Wherever spray drying is used, the operating parameters must be chosen to obtain the desired properties in the final product. For example, when producing detergents it is essential that the finished powder has the correct dissolution rate, requiring the control of physical properties such as density and porosity, [14]. Predicting such properties still presents considerable difficulties to modellers.

The droplet drying sub-model is the key to obtaining final powder properties from spray dryer simulations, [32]. The simplest models are limited to predicting the bulk moisture content of droplets as they dry. Such models may be based on the idea of a characteristic drying curve, [29, 33] or a reaction-engineering approach, [7–9]. Such models have the advantage of being computationally cheap when implemented within computational fluid dynamics (CFD) codes, but provide limited information about the drying droplets. More complicated descriptions based upon the diffusion equation give a spatially resolved moisture fraction, [15, 22], but are still unable to capture the process of solid particle formation. Because droplet drying and particle formation occur simultaneously within a spray drying tower, the drying mechanism and resultant kinetics are strongly inter-dependent on the evolving particle microstructure, [26]. To accurately describe the drying of slurry droplets it is therefore necessary that the drying model is capable of describing the formation of solid particles, as well as giving the bulk moisture content.

Several models capable of describing evolving particle morphology exist in the literature, varying in complexity. Whitaker [59] sets out a comprehensive framework for modelling the drying of porous media including a detailed description of solid, vapour and multi-component continuous phases. A number of authors have applied such methodologies to model physical systems, [*e.g.* 17, 31, 42], but, in general, such a detailed approach is unfeasible, requiring excessive computational time and determination of multiple unknown physical parameters. Consequently, there exist a wealth of simpler models to track the morphological development of drying droplets.

A large variety of morphologies are observed when drying droplets to solid particles, [55, 56], and some of these possibilities are illustrated in **Figure 1**. Identical droplets can dry to small, dense, solid particles or large inflated shells depending on their drying history. Alternatively, two particles subjected to identical drying conditions but with different initial compositions might form particles with markedly different morphologies. Capturing this diversity of possibilities is a challenge when constructing models for single droplet drying; most of the simplified models in the literature are only capable of simulating the production of one particle type.

The most common way to handle particle formation is by a receding-interface, or shrinking core type approach [10, 13, 28, 37]. Such models assume ideal shrinkage initially until a pre-specified critical moisture content is attained. Thereupon, evaporation is said to occur at a clearly defined receding front, separating a wet central core from a dry outer crust with constant properties.

Models with a dry crust are capable of tracking the formation of a dry particle, as well as
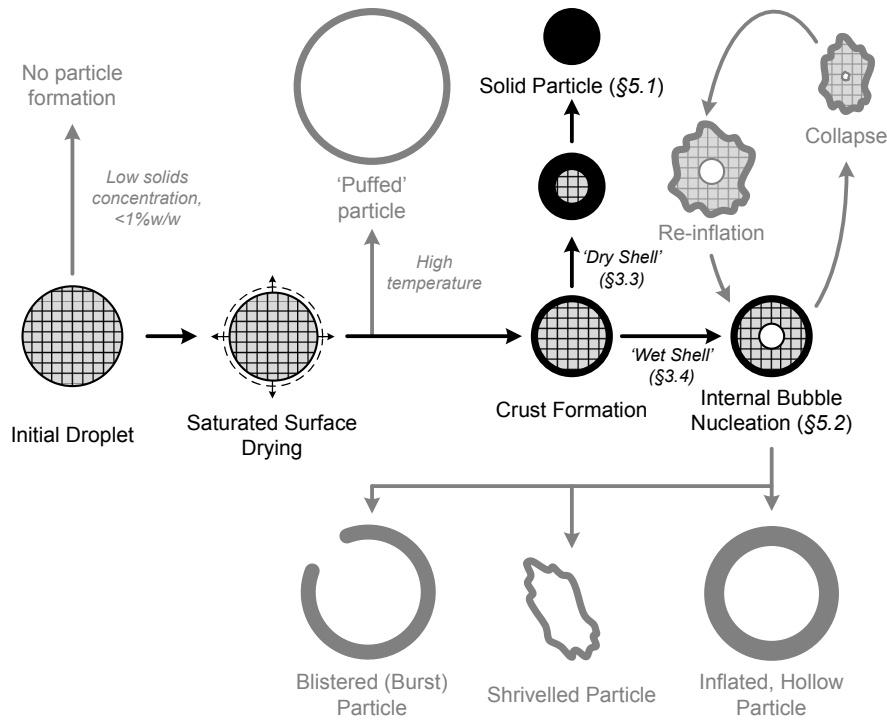
Figure 1: *Schematic showing some of the different particle morphologies that may result when drying droplets containing dissolved or suspended solids. The highlighted portions show the wet and dry shell drying mechanisms discussed in this paper and the particle morphologies that result. Examples of droplets drying to both a solid particle and a hollow shell are presented in Section 5.*

predicting its final size. However, by design they always predict the formation of a solid particle, (Figure 1). A wider range of particle morphologies can be predicted by drying models including a bubble. Such a model was first introduced by Sano and Keey [44] and applied to an evaporating coal slurry by Lee and Law [34]. Etzel et al. [18] later used a similar model to simulate the drying of skim-milk slurries. In contrast to the receding-interface approaches, models with a bubble generally require that the continuous phase continues to wet all the solids throughout drying. A more recent variant on this theme was presented by Seydel et al. [48], whose model included a population balance to describe the solid particles.

In Handscomb et al. [24], a new model was presented for simulating the drying of slurry droplets consisting of an ideal binary solution containing suspended solids. These solids were handled using a population balance approach, enabling the modelling of particle nucleation and growth from the solution. The paper outlined the core model up until the point of the formation of a solid surface shell. However, to enable prediction of final dried particle properties, it is clearly necessary to simulate beyond this point. The **aim of this paper** is therefore to take up from this point and give details of the new drying model after shell formation. Both 'wet' and 'dry' shells are considered; both descriptions are appropriately formulated for incorporation within the new droplet drying framework. For the first time, switching between these drying modes is allowed, as well as — under

4
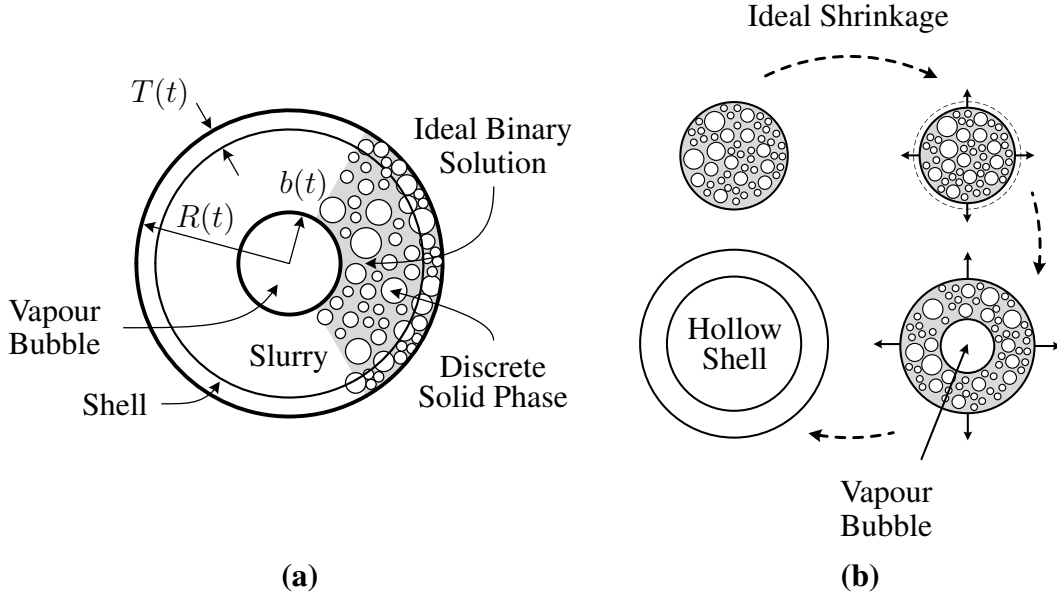
Figure 2: *Schematic showing: (a) the model system; and (b) drying to form a hollow shell.*

certain conditions — continued droplet shrinkage after shell formation. Comparisons with experimental observations from the literature are presented as a means of model validation.

2   Model Review

The present paper considers the drying of droplets consisting of an ideal binary solution containing suspended solids. Following the convention established by Handscomb et al. [24], the solvent, solute and solid will henceforth be labelled A, B and D respectively.

It is assumed that the droplets maintain spherical symmetry throughout their drying history, thus reducing all equations in the final model to a single spatial dimension. Further, the Bîot number is assumed low enough to justify the assumption of a spatially uniform droplet temperature throughout the drying process. The new model contains a centrally located bubble and an explicit shell region, as illustrated in **Figure 2a**. One possible droplet drying history capable of being predicted by the new drying model is illustrated in **Figure 2b**.

2.1   Discrete Phase

The discrete solid phase is modelled by a population of spherical particles, characterised by their diameter, L and radial position within the drying droplet, r. The particle number density, $N(L, r, t)$ evolves in time according to the population balance equation,

$$\frac{\partial}{\partial t}N + \frac{\partial}{\partial L}(GN) + \frac{1}{r^2}\frac{\partial}{\partial r}\left(r^2 v_r^{(d)} N\right) - \frac{1}{r^2}\frac{\partial}{\partial r}\left(r^2 \mathrm{D}\frac{\partial N}{\partial r}\right) = 0\,, \tag{1}$$

5

where the evolution in physical space may occur through a convective or diffusive process. Particle growth occurs at a rate G, which is assumed to be independent of crystal size. Nucleation of particles of size $L_{\min}$ is accommodated through an appropriate boundary condition on the internal coordinate. It is postulated that, once a rigid shell has formed around the droplet, the solid particles are no longer free to move at all within the shell region, *i.e.,* within a rigid shell, particle growth is the sole mechanism operating.

Rather than solving the whole population balance equation, (1), the model evolves the first four integer moments of the internal coordinate, defined by

$$m_a\left(r, t\right) = \int_{L_{\min}}^{\infty} L^a N\left(r, L, t\right) dL, \qquad a \in \{0, 1, 2, 3\}. \tag{2}$$

The evolution of the third moment, m_3, is related to that of the solids volume fraction, ε, by

$$\frac{\partial \varepsilon}{\partial t} = \frac{\pi}{6} \int_{L_{\min}}^{\infty} L^3 \frac{\partial N}{\partial t} dL = \frac{\pi}{6} \frac{\partial m_3}{\partial t}. \tag{3}$$

Integrating (1), invoking standard regularity conditions, gives the general moment evolution equation,

$$\frac{\partial m_a}{\partial t} = L_{\min}^a \dot{N}_0 + aG m_{a-1} + \frac{1}{r^2} \frac{\partial}{\partial r}\left(r^2 D \frac{\partial m_a}{\partial r}\right), \tag{4}$$

where $\dot{N}_0$ is the particle nucleation rate per unit volume.

It is assumed that the solid particles do not leave the droplet. This is captured in the population balance by means of a birth term, giving the external boundary condition as

$$\left.\frac{\partial N}{\partial r}\right|_{r=R} = -\frac{\dot{m}''}{D\rho_A^0} N. \tag{5}$$

Symmetry at the centre gives a zero gradient boundary condition at the internal edge of the domain.

2.2 Continuous Phase Equations

The continuous phase is described by a single equation derived from the volume averaged differential mass balance for the solute and assuming Fickian diffusion for the transport term. Written in terms of the intrinsic volume average of the solute mass fraction taken with respect to the continuous phase, $\langle \omega_B \rangle^{(c)}$, the equation is

$$\frac{\partial}{\partial t}\left[(1 - \varepsilon)\rho^{(c)}\langle \omega_B \rangle^{(c)}\right]$$
$$+ \frac{1}{r^2}\frac{\partial}{\partial r}\left[\underbrace{r^2\left(1 - \varepsilon\right)v_r^{(c)}\rho^{(c)}\langle \omega_B \rangle^{(c)}}_{\text{advection}} - \underbrace{r^2 \mathcal{D}_{\text{eff}}\rho^{(c)}\frac{\partial}{\partial r}\left[(1 - \varepsilon)\langle \omega_B \rangle^{(c)}\right]}_{\text{diffusion}}\right] - r_B'' = 0. \tag{6}$$

$\mathcal{D}_{\text{eff}}$ is an effective diffusion coefficient usually obtained from experiments and, in general, a function of the local moisture content. r_B'' is the volume averaged interfacial production rate of the solute resulting from the crystallisation process. Assuming no volume change on crystallisation, this is easily obtained from the moments of the discrete phase using (4).

The advective velocity, $v_r^{(c)}$, in (6) arises as a result of the density difference between the solute and solvent. Considering volume conservation of the continuous phase therefore allows the following expression to be derived

$$v_r^{(c)} = \mathcal{D}_{\text{eff}} \left(\frac{1}{\Lambda_B + \langle \omega_B \rangle^{(c)}} \frac{\partial \langle \omega_B \rangle^{(c)}}{\partial r} - \frac{1}{1-\varepsilon} \frac{\partial \varepsilon}{\partial r} \right) , \tag{7}$$

where Λ_B is a dimensionless ratio of material densities,

$$\Lambda_B = \frac{\rho_B^0}{\rho_A^0 - \rho_B^0} . \tag{8}$$

It is assumed that the solute does not leave the droplet at any time, *i.e.,* the solute mass flux following the receding interface is zero. The external boundary condition on the solute equation is therefore

$$\left. \frac{\partial \langle \omega_B \rangle^{(c)}}{\partial r} \right|_{r=R} = \frac{\langle \omega_B \rangle^{(c)} \dot{m}''}{\rho^{(c)} \mathcal{D}_{\text{eff}}} , \tag{9}$$

where $\dot{m}''$, the solvent mass flux from the droplet surface, is related to the rate of shrinkage by

$$\frac{dR}{dt} = -\frac{\dot{m}''}{\rho_A^0} . \tag{10}$$

The total rate of solvent evaporation from the droplet, $\dot{m}_{\text{vap}}$ is given by

$$\dot{m}_{\text{vap}} = 4\pi R^2 \dot{m}'' = 2\pi \bar{\rho} \bar{D}_{\text{A,air}} R \, \text{Sh}^* \ln \left(1 + B_m \right) , \tag{11}$$

where $\bar{\rho}$ is the density of the surrounding gas and $\bar{D}_{\text{A,air}}$ is the binary diffusion coefficient of the gas and water vapour. Sh^* is the Sherwood number modified to take account of high mass transport rates from the droplet and B_m is the Spalding mass transfer number, [4, 51]. The algorithm suggested by Abramzon and Sirignano [1] is used to calculate $\dot{m}_{\text{vap}}$, together with the heat penetrating into the drying droplet. From this — and the assumption of no internal temperature gradients — the droplet temperature is evolved.

3   Droplets Drying with a Rigid Shell

The model summarised in the previous section dealt with the simulation of droplets drying prior to the formation of a rigid shell, [24]. In this paper, the model is extended to simulate drying in the presence of a crust and, in conjunction with this, a centrally located bubble is introduced.
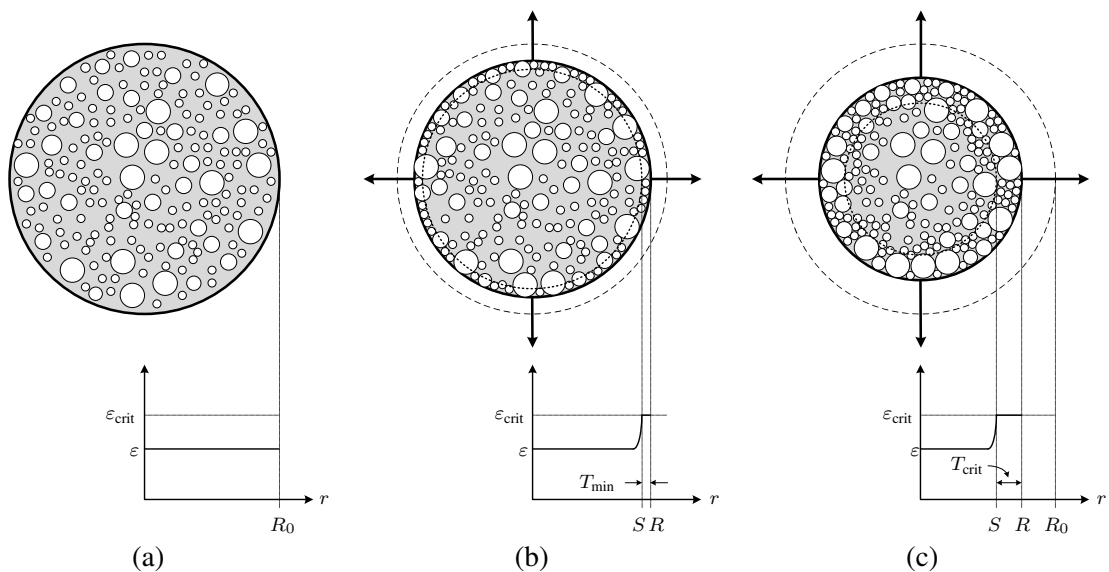
Figure 3: *Schematic illustrating the process of shell thickening: (a) initially the droplet is homogenous and drying proceeds ideally; (b) a shell forms when the maximum packing fraction, ε_{crit}, is reached at the surface of the droplet; (c) the solid particles continue to redistribute — and the droplet continues to shrink — until a critical shell thickness, T_{crit}, is attained.*

3.1 Shell Formation

Initially the suspended solids are assumed to be uniformly distributed within the droplet as illustrated in **Figure 3a**. As the droplet drys the solid particles are drawn inwards by surface tension forces, causing the solids volume fraction at the receding surface to increase. In the new droplet drying model, a shell is deemed to have formed once the volume fraction of particles at the droplet surface rises above a certain critical value, ε_{crit}, (**Figure 3b**). A number of authors [*e.g.* 6, 36] have discussed how the solids particle-size distribution may be used to predict the maximum packing fraction and it is imagined that the information from the population balance could be used to inform the point at which shell formation is deemed to occur. However, for the systems simulated in this paper, ε_{crit} is taken to be a pre-defined parameter.

Most models in the literature, [*e.g.* 16, 28, 47], assume the droplet ceases shrinking as soon as a shell is formed. In reality contraction may continue beyond this point and will only cease when the structural strength of the shell is sufficient to withstand the collapsing forces acting on the droplet arising from continued evaporation, [57]. In many situations it is unlikely that the initial shell — which may be only a few particles thick — will possess sufficient strength. To deal with such situations, the present droplet drying model has provision for a shell thickening regime lying between the initial appearance of a shell and the formation of *rigid* crust. This thickening regime allows for continued shrinkage of the droplet whilst the shell grows to a critical shell thickness, T_{crit}, which represents the balance of structural and capillary forces, (**Figure 3c**).

Once it has formed, the presence of a rigid shell fixes the volume of the drying droplet.

8

Further removal of moisture must lead to an expanding vapour-saturated space somewhere within the droplet. Several workers have investigated the detailed modelling of moisture transport through porous media containing a gas phase, [19, 49, 52], but two limiting cases may be identified [34]. In the *dry shell* model, the vapour space is in the shell itself and an evaporative front recedes through the droplet. In contrast, the *wet shell* model assumes that the shell region is, at all times, wetted by the continuous phase; the vapour now lies in a single, centrally-located, bubble. This paper demonstrates the application of both of these limiting models within the new droplet drying framework and presents a comparison with experimental results for both.

3.2 Shell Thickening

3.2.1 Physics of Shell Thickening

The deformation of the shell during the thickening regime is driven by capillary forces between the suspended particles, [54]. As the continuous phase recedes into the droplet, menisci form between the particles at the surface. These menisci support a pressure drop of

$$\Delta P = \frac{2\gamma}{r_M} \, , \tag{12}$$

where γ is the surface tension and r_M is the radius of curvature of the meniscus. The pressure gradient within the droplet resulting from this capillary pressure leads to transport of the continuous phase towards the outer surface. At the same time, the tension from these menisci drives the particles past each other towards the centre through repeated mini-buckling events. These two processes occur simultaneously and — provided the capillary forces are strong enough — can lead to continued droplet shrinkage after the formation of a surface shell.

At the point of shell formation, the shell thickness, $T_{\min}$, is set equal to the diameter of the smallest of the suspended particles, (Figure 3b). The continuous phase is assumed to continue wetting the surface particles during the thickening regime, which means that evaporation proceeds at the external surface of the droplet. Consequently, the external radius of the particle continues to decrease according to (10). Assuming the volume fraction of solids in the thickening shell remains at the critical value, $\varepsilon_{\mathrm{crit}}$, the inner boundary of this shell at $r = S\left(t\right) = R - T$ must move inwards according to

$$\frac{dS}{dt} = \left(\frac{\varepsilon|_{S^+}}{\varepsilon|_{S^+} - \varepsilon|_{S^-}} \right) \left(\frac{R}{S} \right)^2 \frac{dR}{dt} \, , \qquad \varepsilon|_{S^+} \neq \varepsilon|_{S^-} \ , \tag{13}$$

until it achieves some critical thickness, T_{crit}, (Figure 3c).

In order to say when the droplet stops shrinking, it is necessary to determine when the thickening shell becomes structurally capable of supporting itself. As stated above, the continued deformation of the shell is hypothesised to occur through a series of mini-buckling events driven by the capillary pressure of the receding continuous phase. Timoshenko [53] showed that a spherical shell of radius R and thickness T will buckle when

9
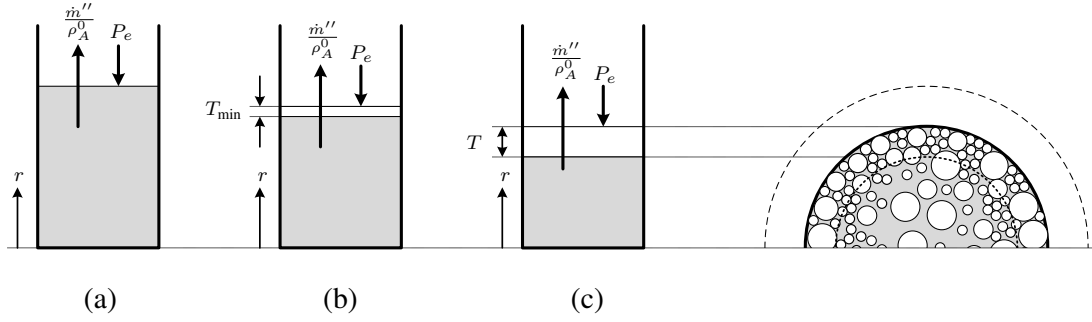
Figure 4: *Schematic demonstrating how the process of shell thickening can be likened to the growth of a filter cake: (a) Prior to shell formation; (b) the point of shell formation corresponds with the appearance of a filter cake one particle thick; (c) the filter cake thickness, T continues to increase as the shell grows. The volumetric flow through the filter cake is simply related to the mass flux from the droplet, $\dot{m}''$, and results in a pseudo-pressure acting on the shell, P_e.*

subjected to a uniform external pressure, P_{buck}, given by

$$P_{\text{buck}} = \left(\frac{T}{R-T}\right)^2 \frac{2E}{\sqrt{3\left(1-\nu^2\right)}} \, , \qquad (14)$$

where E is the Young's modulus of the material and ν is its Poisson's ratio. It is hypothesised that the newly formed shell will continue to experience buckling events — and therefore continue to thicken — so long as the capillary pressure is greater than the buckling pressure, P_{buck}.

To determine the capillary pressure, the movement of the continuous phase through the shell is likened to filtration through a porous filter with the same thickness as the growing crust [38]. The pressure drop across the shell will be equal to the pressure drop across the air–continuous phase interface, given by (12). This analogy is illustrated schematically in **Figure 4**.

Assuming the filter to be incompressible, Darcy's law may be used to obtain the pressure drop across the growing shell required to produce a given fluid flow,

$$\kappa\frac{\Delta P}{\mu T} = \frac{dR}{dt} = \frac{\dot{m}''}{\rho_A^0} \, , \qquad (15)$$

where κ is the permeability of the shell. Here the fluid flow has been expressed in terms of the mass flux of solvent from the particle, $\dot{m}''$, which is simply related to the rate of shrinkage by (10). The permeability is estimated using the Carmen-Kozeny relation, [11],

$$\kappa = \frac{1}{180}\frac{(1-\varepsilon)^3}{\varepsilon^2}L^2 \, . \qquad (16)$$

In the above expression, L is the diameter of the solid particles — assumed spherical — making up the porous medium. In the current model, the first moment of the population balance, m_1, is used as this represents the local average solid particle size.

10

The pressure drop across the shell, equal to the pressure drop across the air–continuous phase interface, can be thought of as exerting an external pseudo-pressure, P_e, on the thickening shell. The shell will continue to thicken so long as this pseudo-pressure is greater than the pressure required to cause buckling of the shell. That is, whilst

$$\frac{(2R-T)^2}{T}\dot{m}'' > \frac{\rho_A^0}{\mu}\frac{8E\kappa}{\sqrt{3\left(1-\nu^2\right)}}\ ,\tag{17}$$

where the terms on the right of the inequality are approximately constant for a given system. This gives a way of calculating the extent of shell thickening without needing to specify a maximum thickness in advance of the simulation. In turn, this determines the droplet size at which shrinkage ceases. The drying conditions affect the evaporative flux, $\dot{m}''$, and will thus directly influence the final particle size.

3.2.2 Implementation of Shell Thickening in the Present Model

The continuous phase continues to wet the shell during the thickening regime and consequently the equation which describes the behaviour of this phase, (6), is unchanged. In contrast, the solids within the thickening shell now behave differently.

In the thickening regime, the solute boundary condition at the external droplet surface, (9), remains unchanged. However, the appropriate boundary conditions to be implemented at the internal surface of the thickening shell are more complicated. Considering the superficial solute flux at $r = S$ gives

$$\left.\overline{n}_{Br}^{(c)}\right|_{r=S} = (1-\varepsilon)\left.\langle n_{Br}\rangle^{(c)}\right|_{r=S} = (1-\varepsilon)\,v_r^{(c)}\rho^{(c)}\langle\omega_B\rangle^{(c)} - \mathcal{D}_{\text{eff}}\rho^{(c)}\frac{\partial}{\partial r}\left[(1-\varepsilon)\langle\omega_B\rangle^{(c)}\right]$$

$$\tag{18a}$$

$$= (1-\varepsilon)\left.\langle n_{Br}\rangle^{(c)}\right|_{r=S(t)} + \rho^{(c)}(1-\varepsilon)\langle\omega_B\rangle^{(c)}\frac{dS}{dt}\ ,$$
$$\tag{18b}$$

which, on substituting for $v_r^{(c)}$ from (7) may be rearranged to give

$$\frac{\partial\langle\omega_B\rangle^{(c)}}{\partial r} = -\frac{\rho_A^0}{\mathcal{D}_{\text{eff}}\rho^{(c)}}\left[\langle\omega_B\rangle^{(c)}\frac{dS}{dt} + \frac{\left.\langle n_{Br}\rangle^{(c)}\right|_{r=S(t)}}{\rho^{(c)}}\right]\ .\tag{19}$$

Note that the intrinsic solute mass fraction and, consequently, the continuous phase density must the same either side of the inner shell wall at $r = S$. Further, the solute mass flux across the growing shell boundary must be continuous, that is, we require both

$$\left.\langle\omega_B\rangle^{(c)}\right|_{r=S^+} = \left.\langle\omega_B\rangle^{(c)}\right|_{r=S^-}\tag{20a}$$

and

$$\left.\overline{n}_{Br}^{(c)}\right|_{r=S^-(t)} = \left.\overline{n}_{Br}^{(c)}\right|_{r=S^+(t)}$$

$$\Rightarrow \left.\langle n_{Br}\rangle^{(c)}\right|_{r=S^+(t)} = \left(\frac{1-\varepsilon^-}{1-\varepsilon^+}\right)\left.\langle n_{Br}\rangle^{(c)}\right|_{r=S^-(t)}\ .\tag{20b}$$

11

In these last two equations, $S^- = S - \delta r$ represents a radial location just inside the thickening shell, and $S^+ = S + \delta r$ a location just outside.

Equation (19) may now be evaluated at both S^- and S^+ which, on substitution into (20b), can then be rearranged to give a relationship between the solute mass fraction gradients on either side of the growing shell interface,

$$\frac{\partial \langle \omega_B \rangle^{(c)}}{\partial r}\bigg|_{r=S^-} = \frac{\mathcal{D}_{\text{eff}}^+}{\mathcal{D}_{\text{eff}}^-} \left(\frac{1 - \varepsilon^+}{1 - \varepsilon^-} \right) \frac{\partial \langle \omega_B \rangle^{(c)}}{\partial r}\bigg|_{r=S^+} - \frac{\rho_A^0 \langle \omega_B \rangle^{(c)}}{\mathcal{D}_{\text{eff}}^- \rho^{(c)}} \left(\frac{\varepsilon^- - \varepsilon^+}{1 - \varepsilon^-} \right) \frac{dS}{dt} \ . \quad (21)$$

This, along with (20a), gives the required two boundary conditions for the solute equation at the shell interface.

During the thickening regime, the particles in the shell are rearranging themselves as the crust deforms. The model allows for continued solids growth during this period, but does not seek to model the precise nature of the spatial rearrangement. Rather it is assumed that the solid particles are no longer free to diffuse but are subjected to an imposed velocity,

$$v_r^{(d)} = \left(\frac{R}{r} \right)^2 \frac{dR}{dt} \quad (22)$$

arising from the deforming shell. Equation (1) therefore reduces to

$$\frac{\partial}{\partial t} N + \frac{\partial}{\partial L} (GN) + \left(\frac{R}{r} \right)^2 \frac{dR}{dt} \frac{\partial N}{\partial r} = 0 \ , \quad (23)$$

in the thickening shell. The appropriate boundary conditions on this equation are those of zero spatial gradient at both ends.

3.3 Dry Shell Model

3.3.1 Model Description

The dry shell model is, in its simplest form, a classical shrinking core type analysis whereby a central core of wetted material contracts as moisture evaporates from a receding interface, [2, 10]. The dry shell is defined to be the region beyond this wetted core. As suggested by **Figure 1**, droplets drying via this dry shell route might be expected to form solid particles or, at high temperatures, they might shatter. Although the initiation of shell formation may be signalled by some critical solids volume fraction at the droplet surface, it is noted that the dry shell model *does not* explicitly place a requirement on the solids volume fraction within the growing shell region. The porosity of dry shell particles might therefore be expected to vary — perhaps considerably — with position. In contrast to several previous implementations which assumed constant dry crust properties, [*e.g.* 10, 13], porosity variations in the dry shell are tracked in the present model.

In the present implementation of the dry shell model, the shell is assumed to be *completely* dry, that is, there is no solvent *or* solute remaining in the crust region. Further, it is assumed that there is no vapour in the wet core and, consequently, the continuous phase
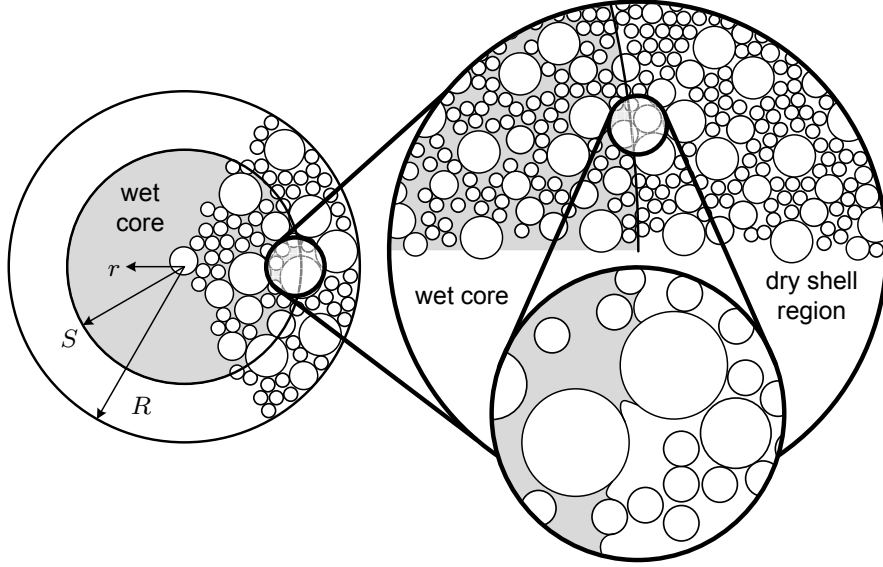
Figure 5: *Illustration of a droplet of radius, R drying through a dry shell with internal radius, S. The shell region is completely dry, containing no solvent or solute. The wet core remains free of vapour and thus the continuous phase remains funicular throughout drying.*

remains funicular throughout drying, [30]. This is illustrated schematically in **Figure 5**. Within the wet core, the equations to be solved for the solute mass fraction and the moments of the population balance are the same as outlined in Section 2. As demonstrated in the example below, continuing to solve these equations in the wet region allows the properties of the growing dry crust to be predicted.

3.3.2 Shell Growth

The dry shell is assumed to grow according to

$$\frac{dS}{dt} = -\left(\frac{R}{S}\right)^2 \frac{\dot{m}''}{\rho_A^0 \left(1 - \varepsilon|_S\right)} \, , \tag{24}$$

where the solids volume fraction is evaluated at the receding interface, $r = S$. The ratio of radii accounts for the fact that $\dot{m}''$ still refers to the evaporative solvent flux at the external surface of the droplet. The presence of a dry shell adds an additional mass transfer resistance, [27], characterised in this model by an effective diffusion coefficient of the solvent vapour through the dried shell region, D_{eff}. This may be related to the binary diffusion coefficient of water in air, $\bar{D}_{\text{A,air}}$, via

$$D_{\text{eff}} = \frac{(1 - \varepsilon) \, \bar{D}_{\text{A,air}}}{\sigma} \, , \tag{25}$$

where σ is the tortuosity of the porous shell, [12]. The additional resistance provided by the dried shell acts in series with the existing external mass transfer resistance, (11), to

give a revised expression for the mass flux of moisture from the drying droplet

$$\dot{m}_{\mathrm{vap}} = 4\pi R^2 \dot{m}'' = 2\pi \bar{\rho} \, \bar{D}_{\mathrm{A,air}} R \left[\frac{\bar{D}_{\mathrm{A,air}}}{D_{\mathrm{eff}}} \left(\frac{S-R}{2S} \right) + \frac{1}{\mathrm{Sh}^*} \right]^{-1} \ln\left(1 + B_m\right) . \qquad (26)$$

Note that this reduces to (11) when $S = R$.

If the temperature of the drying air is above the boiling point of the continuous phase then boiling might occur. This is easily incorporated within the dry shell framework. Assuming that all energy supplied to the droplet in the boiling regime is used to vaporise the continuous phase, (26) is modified to read

$$\dot{m}_{\mathrm{vap}} = 4\pi R^2 \dot{m}'' = \frac{Q}{\Delta H^{\mathrm{vap}}} , \qquad (27)$$

where Q is the heat penetrating into the droplet and ΔH^{vap} is the latent heat of vaporisation of the continuous phase. The dry shell growth rate in the boiling regime is still obtained from (24) with $\dot{m}''$ now given by (27).

3.3.3 Boundary Conditions

The symmetry boundary conditions in the centre of the droplet remain unchanged once a dry shell has formed. However, the external boundary conditions, now at $r = S(t)$, require modification. The solute boundary condition at this outer edge of the wet central core becomes

$$\left. \frac{\partial \langle \omega_B \rangle^{(c)}}{\partial r} \right|_{r=S} = \frac{\langle \omega_B \rangle^{(c)} \dot{m}''}{\rho^{(c)} \mathcal{D}_{\mathrm{eff}} \left(1 - \varepsilon|_S\right)} , \qquad (28)$$

where $\dot{m}''$ is given by (26). Comparison with (9) shows that the only difference from the external solute boundary condition prior to shell formation is the inclusion of the $\left(1 - \varepsilon|_S\right)^{-1}$ term. The outer boundary condition on the moment system is now

$$\left. \frac{\partial N}{\partial r} \right|_{r=R} = 0 , \qquad (29)$$

as no solids are allowed to enter or leave the dried region. This completes the description of the dry shell model.

3.4 Wet Shell Model

3.4.1 Model Description

The key assumption of the wet shell model is that the solids in the shell region remain wetted by the continuous phase and, consequently, the evaporative front remains at the droplet surface. As discussed above, continued solvent evaporation from an unshrinking droplet requires the presence of a growing vapour space. In the wet shell model, this takes the form of a single, centrally located bubble, as illustrated in **Figure 6**.
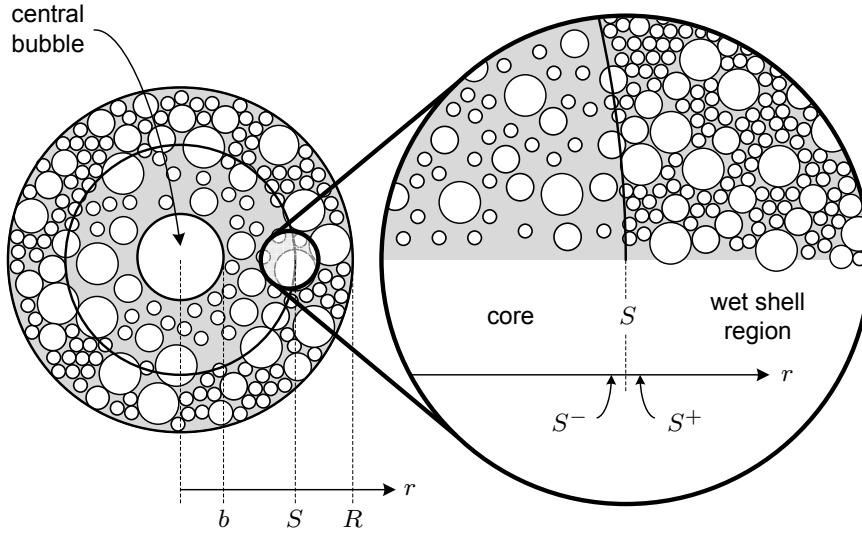
Figure 6: *Illustration of a droplet of radius, R drying through a wet shell with internal radius, S. The solid particles in the wet shell remain wetted by the continuous phase and a central bubble grows as evaporation proceeds.*

As the continuous phase wets all the solid particles in this model, the shell itself cannot be identified in terms of a dry region as was done in the dry shell model. Instead the shell is defined as the region which has a solids volume fraction higher than some critical value. This value is normally taken to be the same as the critical solids volume fraction triggering shell formation, $\varepsilon_{\text{crit}}$, although it is noted that this need not be the case. Figure 6 demonstrates how the droplet is divided into the core and wet shell regions, separated by the internal edge of the growing shell at $r = S$.

Volume conservation requires that the rate of growth of the central bubble must be related to the evaporative moisture flux according to

$$\frac{db}{dt} = \frac{R^2}{b^2} \frac{\dot{m}''}{\rho_A^0} \,, \qquad b > 0 \,. \tag{30}$$

From this expression, it is clear that a seed bubble of finite size is required to avoid an infinite initial growth rate. Physically, this is likely to be an air bubble present in the feed material or introduced during spraying. The central bubble is filled with vapour saturated drying air, *not* pure solvent vapour. That is, the partial pressure of solvent in the bubble will be in equilibrium with that in the adjacent droplet. As the bubble grows, it is assumed that the mass of solvent in the bubble remains small compared to the amount in the surrounding droplet. Consequently, the moisture flux to the bubble is negligible and has no effect on the surrounding concentration gradients.

During the thickening period, the shell undergoes mini-buckling events due to the stresses resulting from capillary pressure. As is clear from (12), this pressure will be greatest in the narrowest pores. Indeed, it is well known that larger pores will preferentially drain whilst the narrower pores stay filled with liquid, Keey [29], Scherer [45]. The draining of these wider pores during the thickening period provides a route through which drying air

can enter the central bubble which grows in the wet shell regime.

The growing bubble is modelled as imposing an outward advective velocity on the droplet. The bulk continuous-phase velocity, (7), is modified to read

$$v_r^{(c)} = \mathcal{D}_{\text{eff}} \left(\frac{1}{\Lambda_B + \langle \omega_B \rangle^{(c)}} \frac{\partial \langle \omega_B \rangle^{(c)}}{\partial r} - \frac{1}{1 - \varepsilon} \frac{\partial \varepsilon}{\partial r} \right) + \frac{b^2}{r^2} \frac{db}{dt} , \tag{31}$$

where the final term is the additional advective component due to the bubble. With this modification to $v_r^{(c)}$, the continuous phase equation, (6), can be applied without further alteration in both the shell and core regions.

The evolution equation for the population of solid particles, (1), has the same additional advective component as a result of the growing bubble. The equation describing the solids in the core region is therefore now

$$\frac{\partial}{\partial t} N + \frac{\partial}{\partial L} (GN) + \frac{b^2}{r^2} \frac{db}{dt} \frac{\partial N}{\partial r} - \frac{1}{r^2} \frac{\partial}{\partial r} \left(r^2 D \frac{\partial N}{\partial r} \right) = 0 . \tag{32}$$

Within the shell region, the solid particles are no longer free to move at all. The population only evolves due to crystallisation from the continuous phase and (1) reduces to

$$\frac{\partial}{\partial t} N + \frac{\partial}{\partial L} (GN) = 0 . \tag{33}$$

Nucleation of new particles within the wet shell is possible, but this is thermodynamically unlikely in a region which, by definition, already has a high volume fraction of solids. Nucleation has therefore neglected.

3.4.2 Shell Growth

The shell grows as a result of solid particles depositing on the inside wall at $r = S^-$. From (32) it is seen that the particle number density flux in the space of the external coordinate is given by

$$\dot{N}_r = \frac{b^2}{r^2} \frac{db}{dt} N - D \frac{\partial N}{\partial r} . \tag{34}$$

If the advective flux of solids is assumed to dominate the deposition process, then

$$\dot{N}_r \approx \frac{b^2}{r^2} \frac{db}{dt} N , \tag{35}$$

and so, following the growing shell interface at $r = S(t)$, it is possible to write

$$N^- \frac{b^2}{S^2} \frac{db}{dt} = \left(N^- - N^+ \right) \frac{dS}{dt} . \tag{36}$$

Here N^- and N^+ represent the particle number density at S^- and S^+ respectively. Rearranged, this gives the shell growth rate as

$$\frac{dS}{dt} = -\frac{b^2}{S^2} \frac{db}{dt} \frac{N^-}{(N^+ - N^-)} . \tag{37}$$

Note that this expression implies that the gradient of the particle number density is zero at the shell interface, *i.e.,*

$$\left.\frac{\partial N}{\partial r}\right|_{r=S^-} = 0 \ . \tag{38}$$

This might be viewed as unrealistic as the growing boundary also acts as a sink for diffusing solid particles. This effect can be captured through the incorporation of a *sink diffusion* term [25, 60]. Assuming that the rate of sink diffusion may be modelled by the simple model

$$\dot{N}_{\text{sink}} = k_{\text{sink}} N \ , \tag{39}$$

which, included in (35) gives a new solids flux to the growing wall,

$$\dot{N}_r = \frac{b^2}{S^2}\frac{db}{dt}N + k_{\text{sink}}N \ . \tag{40}$$

The wet shell growth rate is then modified to read

$$\frac{dS}{dt} = \frac{-N^-}{N^+ - N^-}\left(\frac{b^2}{S^2}\frac{db}{dt} + k_{\text{sink}}\right) \ , \tag{41}$$

which, in terms of the moments, (4), is

$$\frac{dS}{dt} = \frac{-m_a^-}{m_a^+ - m_a^-}\left(\frac{b^2}{S^2}\frac{db}{dt} + k_{\text{sink}}\right) \ . \tag{42}$$

3.4.3 Boundary Conditions

From the definition of the wet shell region, it is clear that the appropriate boundary condition for the solids volume fraction at $r = S^+$ is

$$\varepsilon^+ = \varepsilon_{\text{crit}} \ . \tag{43a}$$

Rearranging (42) then gives the boundary conditions for the remaining moments

$$m_a^+ = m_a^-\left[1 - \left(\frac{b^2}{S^2}\frac{db}{dt} + k_{\text{sink}}\right)\left(\frac{dS}{dt}\right)^{-1}\right] \ , \qquad a \in \{0, 1, 2\} \ , \tag{43b}$$

and the shell growth rate is

$$\frac{dS}{dt} = \frac{-\varepsilon^-}{\varepsilon_{\text{crit}} - \varepsilon^-}\left(\frac{b^2}{S^2}\frac{db}{dt} + k_{\text{sink}}\right) \ . \tag{44}$$

The solute boundary condition at the external droplet surface remains unchanged, *i.e.,* equation (9) is still used. The appropriate boundary conditions to be implemented at the internal surface of the wet shell are similar to those in the thickening shell, as discussed in Section 3.2. Due to the modification to $v_r^{(c)}$, (19) becomes

$$\frac{\partial \langle \omega_B \rangle^{(c)}}{\partial r} = -\frac{\rho_A^0}{\mathcal{D}_{\text{eff}}\rho^{(c)}}\left[\langle \omega_B \rangle^{(c)}\underbrace{\left(\frac{dS}{dt} - \frac{b^2}{S^2}\frac{db}{dt}\right)}_{v_s} + \frac{\langle n_{Br}\rangle^{(c)}\big|_{r=S(t)}}{\rho^{(c)}}\right] \ , \tag{45}$$

which, on imposing continuity of the solute mass flux across the growing shell and rearranging as above gives the boundary condition

$$\left.\frac{\partial \langle \omega_B \rangle^{(c)}}{\partial r}\right|_{r=S^-} = \frac{\mathcal{D}_{\text{eff}}^+}{\mathcal{D}_{\text{eff}}^-}\left(\frac{1-\varepsilon^+}{1-\varepsilon^-}\right)\left.\frac{\partial \langle \omega_B \rangle^{(c)}}{\partial r}\right|_{r=S^+} - \frac{\rho_A^0 \langle \omega_B \rangle^{(c)}}{\mathcal{D}_{\text{eff}}^- \rho^{(c)}}\left(\frac{\varepsilon^- - \varepsilon^+}{1-\varepsilon^-}\right)v_s . \quad (46a)$$

Further, solute mass fraction continuity across this shell edge at $r = S$ gives the second boundary condition,

$$\langle \omega_B \rangle^{(c)-} = \langle \omega_B \rangle^{(c)+} . \quad (46b)$$

A zero gradient boundary condition is applied to all equations at the bubble interface at $r = b$.

3.4.4 Wet Shell to Dry Shell Switch

From the formulation of the wet shell model it is clear that, at some point, the expanding bubble will meet the retreating inner wet shell surface. At this point, the bubble can expand no further and further moisture removal necessitates drying of the shell itself. The new model executes a switch from wet shell to dry shell drying when $b = S$. The equations implemented after this switch are those introduced in Section 3.3. The model is therefore capable of simulating the drying of the shell region following bubble growth. An example of this behaviour is presented in Section 5.2.

4 Implementation

The model as described consists of a set of advection-diffusion equations coupled to ordinary differential equations describing the particle size and temperature. These were solved using the standard NAG Fortran `D03PFF` library routine, [40], which implements an algorithm developed by Pennington and Berzins [41] when supplied with a user-defined switching-upwind numerical flux function. Details of the numerical implementation will appear in a separate paper.

The physical extent of the droplet changes during drying due to both shrinkage and, although not discussed in this paper, bubble growth. In the thickening regime or after formation of a wet shell, an additional coordinate system is introduced to cover this outer region. The extent of this second coordinate system also varies with time. To handle the resulting moving boundary problem, the following coordinate transformation is applied to all equations,

$$z = \frac{r - r_{\text{L}}}{r_{\text{R}} - r_{\text{L}}} \quad ; \quad \frac{\partial}{\partial r} = \frac{1}{r_{\text{R}} - r_{\text{L}}}\frac{\partial}{\partial z} , \quad (47)$$

where, $[r_{\text{L}}, r_{\text{R}}] = [b, S]$ for the internal coordinate system and $[r_{\text{L}}, r_{\text{R}}] = [S, R]$ for the shell region. This transformation has the effect of non-dimensionalising the spatial coordinate and fixing both internal and shell domains on the interval $z \in [0, 1]$, as illustrated in **Figure 7**. Time derivatives in the z coordinate systems are related to those in the r

coordinate system by

$$\left.\frac{\partial}{\partial t}\right|_r = \left.\frac{\partial}{\partial t}\right|_z - \frac{1}{r_\mathrm{R} - r_\mathrm{L}}\left[\frac{dr_\mathrm{L}}{dt} + z\left(\frac{dr_\mathrm{R}}{dt} - \frac{dr_\mathrm{L}}{dt}\right)\right]\frac{\partial}{\partial z}. \tag{48}$$

The transformation is seen to add a virtual flux to all the partial differential equations in the model. A full listing of the model equations after applying this transformation is given in Appendix A.
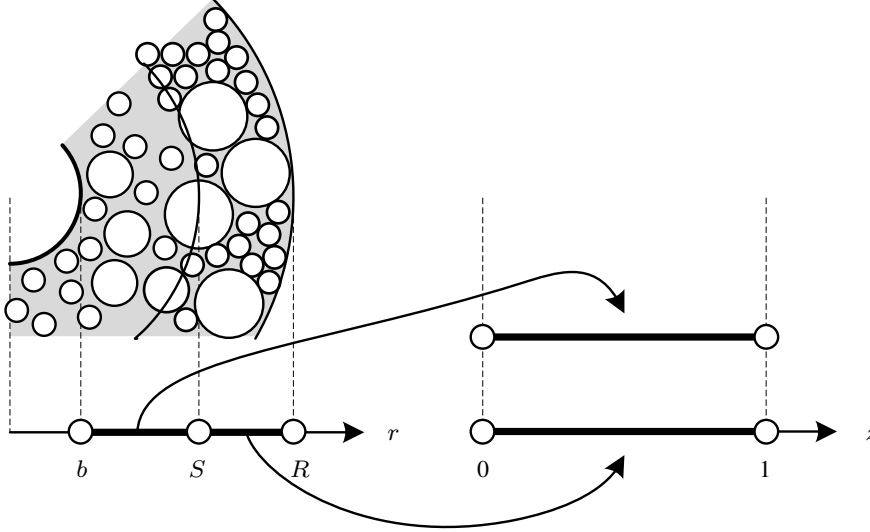

Figure 7: *Illustration of the coordinate transformation applied to a drying droplet with a shell region. After transforming, the core and shell regions are both fixed on the interval $z \in [0, 1]$.*

Droplet drying in the presence of a dry shell does not require a second coordinate system. The dry shell is free of the continuous phase and the particle number density is no longer free to evolve in either its internal or external coordinate. Instead, the properties of the dry shell are stored as the interface recedes and, from this, shell-region profiles can be reconstructed by spline interpolation if required.

5 Results

Two physical systems are simulated using the new model and the results obtained compared with experimental data from the literature. Both examples presented focus on aspects of the model relating to shell formation and the subsequent drying behaviour. A thorough description of the population balance aspects of the model can be found in an earlier paper, [24].

19
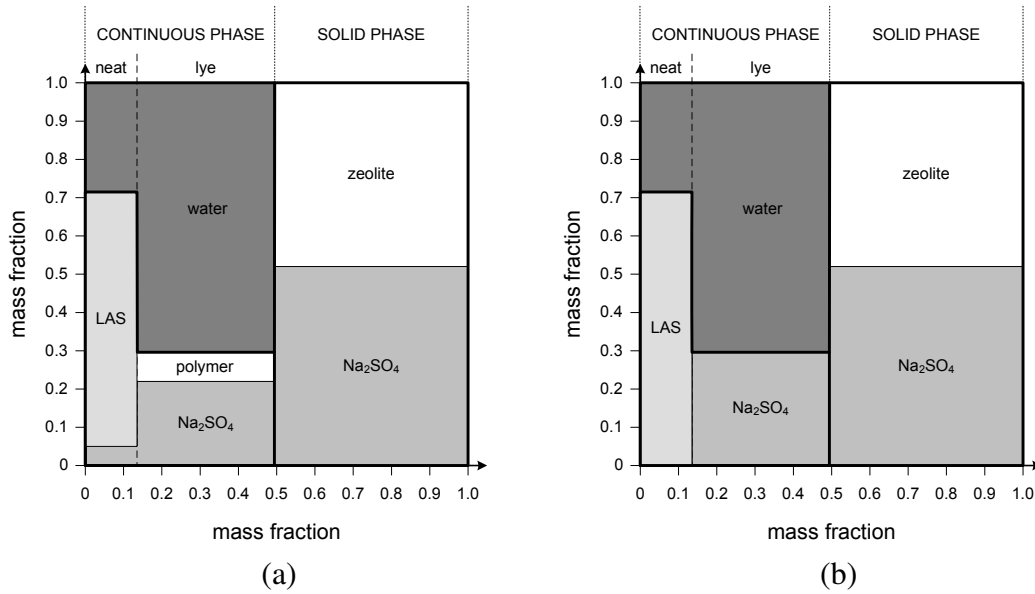
Figure 8: *(a) Initial composition of the crutcher mix droplets as measured by Griffith et al. [21]; and (b) simplified description of the crutcher mix used to model the system in this paper.*

5.1 Drying a Droplet of Detergent Slurry

The first test case is the simulation of a droplet of detergent slurry drying. Such 'crutcher mix' is typically a complex mixture of over 30 components, with precise formulations being closely guarded commercial secrets, [14]. Griffith et al. [22] have recently conducted a series of experiments investigating the drying of a generic crutcher mix formulation, the composition of which is shown in **Table 1**. Griffith et al. report that the droplets they observed showed no shrinkage during drying which indicates that this system might be a suitable choice to demonstrate the dry-shell model.

Table 1: *The composition of the detergent slurry investigated by Griffith et al. [22].*

Component	Initial Mass Fraction
LAS	0.09
Water	0.29
Acusol Polymer	0.03
Sodium Sulphate	0.35
Sodium Aluminosilicate	0.24

The description of the system needs to be further simplified before the the present model can be used. Griffith et al. report that the continuous 'phase' actually comprised individual neat and lye phases which were rich in LAS and sodium sulphate respectively. This is illustrated in **Figure 8a**. To simulate this system within the present framework, the lye phase was modelled as an aqueous sodium sulphate solution. Similarly, the small amount of sodium sulphate in the neat phase is ignored and this is considered to be a LAS–water binary. This further simplified system is illustrated **Figure 8b**.

In terms of the present model, the solid phase, D, comprises the zeolite — sodium aluminosilicate — and some crystallised sodium sulphate and the water in the system is the solvent, A. The LAS and dissolved sodium sulphate must be described as component B. For the remainder of this section, these two components will collectively be referred to as the 'solute'. However, since only sodium sulphate crystallises to form new solid, it is important to track the mass fraction of the combined solute that is Na_2SO_4, *i.e.,*

$$\xi = \frac{\text{mass of Sodium Sulphate}}{\text{mass of Sodium Sulphate} + \text{mass of LAS}} \ . \tag{49}$$

Because of the simplifying assumptions made above, ξ also represents the mass fraction of the solute in the lye phase. Assuming that this fraction is uniform throughout the droplet allows ξ to be simply calculated from the initial masses and knowledge of the mass of Na_2SO_4 that has crystallised during the drying period. This assumption is justifiable as the rate of moisture removal is slow when drying at $T_{gas} = 60°C$. For the droplets observed by Griffith et al. [22], $\xi(t = 0) = 0.56$.

NMR results obtained by Griffith et al. [21] demonstrate that when drying crutcher mix, water is initially lost from the lye phase. Assuming that the ratio of LAS to water in the neat phase remains unchanged until the lye phase has dried allows the mass concentration of sodium sulphate in the lye phase, $\omega_{Na}^{(c)}$, to be determined from ξ:

$$\omega_{Na}^{(c)} = \frac{\xi \langle \omega_B \rangle^{(c)}}{1 - 1.43 \langle \omega_B \rangle^{(c)} (1 - \xi)} \ . \tag{50}$$

Initially, $\omega_{Na}^{(c)} = 0.31$, which is the saturated mass fraction at $60°C$, [58]. This is to be expected as the aqueous and crystallised sodium sulphate are initially in equilibrium. As the drying proceeds sodium sulphate crystallises out of solution. In the absence of any data relating to the model crutcher mix system, the kinetics used to describe this process are those for direct crystallisation to the solid in a sodium sulphate—water mixture. Rosenblatt et al. [43] give the following expression,

$$\frac{dL}{dt} = 1.484 \times 10^7 \exp\left(-\frac{13.7 \times 10^3}{RT}\right) (C_i - C_{eqm})^{1.5} \ , \tag{51}$$

which corresponds to the linear growth rate, G, in the population balance equation (1). C_i and C_{eqm} are the local and saturated sodium sulphate concentrations respectively in $kmol \, m^{-3}$.

As demonstrated in Handscomb et al. [24], the moment system describing the solid phase, (4), allows nucleation of new particles to be modelled. However, the presence of a considerable amount of crystallised sodium sulphate at the outset of drying in the current system makes nucleation of new crystals thermodynamically unlikely. Therefore, the nucleation rate, $\dot{N}_0$, is set to zero in this simulation.

The solids contained in the crutcher mix droplets are relatively large — typically $10 \, \mu m$ in diameter — and, consequently, are relatively immobile. The single, non-size dependent, solids diffusion coefficient was used $D = 10^{-15} \, m^2s^{-1}$.
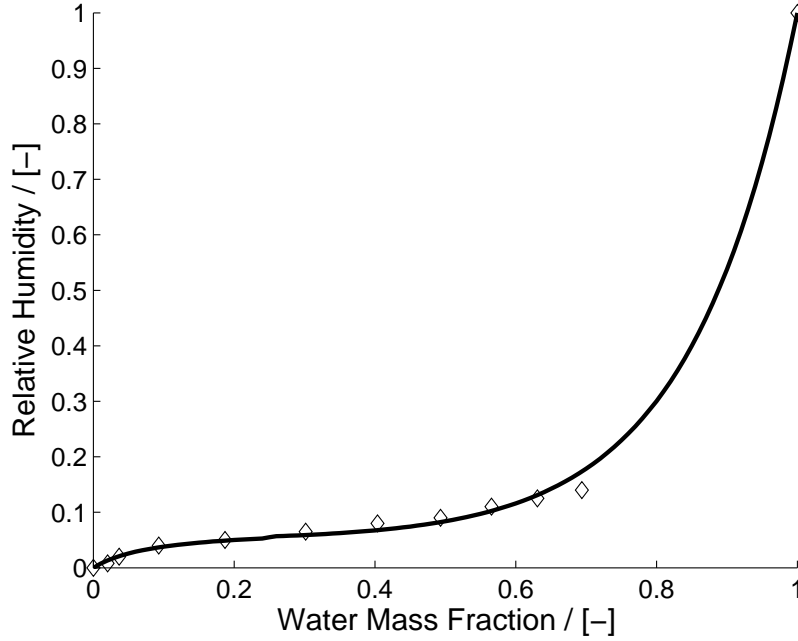
Figure 9: *Water sorption isotherm for crutcher mix. The line shows the sorption isotherm, (53), obtained by fitting to the experimental points obtained by Bayly [3].*

Griffith et al. [22] determined an effective diffusion coefficient appropriate for modelling the movement of water in crutcher mix,

$$\mathcal{D}_{\text{eff}} = \exp\left(-\frac{27.5 + 174.5u}{1 + 8.5u}\right) ,\tag{52}$$

which, as expected, is a strong function of the dry mass basis moisture content, u. The sorption isotherm is required to determine the rate of moisture evaporation to the bulk, (11). This was obtained by fitting a standard sorption isotherm to measurements on the crutcher mix obtained by Bayly [3]. The resulting isotherm is

$$\mathcal{H}_R = \frac{p_A}{p^{\text{sat}}} = f\left(\omega_A\right)\left[\frac{0.8\,\omega_A}{1 + 11\omega_A}\right] + \left(1 - f\left(\omega_A\right)\right)\left[0.05 + \exp\left(\frac{\omega_A - 3.92}{0.15}\right)\right] ,\tag{53}$$

where

$$f\left(\omega_A\right) = \frac{1}{2}\left[1 - \tanh\left(100\pi\left(\omega_A - 0.25\right)\right)\right]\tag{54}$$

is a blending function required to join the different functional forms fitted at high and low moisture contents. The isotherm is plotted in **Figure 9**.

A crutcher mix droplet with an initial diameter of 1.5 mm was simulated drying in dehumidified air at 60°C with a relative velocity of 1.68 ms^{-1}. **Figure 10** shows the simulated moisture mass fraction compared with experimental measurements of a droplet drying under these conditions from Griffith [20]. The simulated moisture content matches the experimental results very well, although the errors associated with the data were not reported.
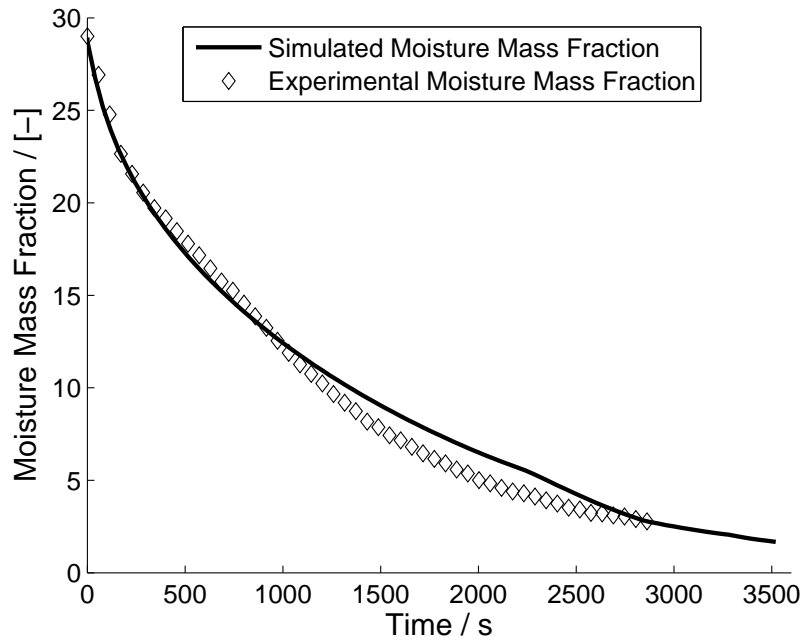
Figure 10: *Simulated evolution of the moisture mass fraction in a crutcher mix droplet (line) compared with experimentally measured values from Griffith [20], (points).*

The use of NMR techniques to follow the droplet drying by Griffith [20] allows for further validation of the current model. **Figure 11** shows a comparison between experimentally measured moisture profiles and those extracted from the simulation after applying an Abel transform, [5]. The NMR data returns intensity readings in arbitrary units. Therefore, assuming an initially homogeneous spherical particle, an appropriate scaling factor was determined and applied to all the simulated profiles. It is clear that the experimental droplet wasn't a perfect sphere, but the error associated with this approximation is small.

The model fit to the measured profiles is fair. The intensity maxima at the centre of the droplet are very well predicted for the 10 and 20 minute profiles, but the predicted profile at 30 minutes does not match the data so well. Between 20 and 40 minutes, the experimental data shows faster drying than predicted by the model as is demonstrated by the observation that the 30 minutes data coincides with the 40 minutes predicted profile. It is possible that this discrepancy is a result of the experimental data which appears to show particularly fast drying between 20 and 40 minutes. However it could also be that the dry shell assumption used in the model is not entirely compatible with this system.

Figure 11 clearly shows the influence of the dry shell assumption in the model results. A dry shell contains no moisture and consequently no NMR signal would be observed from such a region. The simulated profiles reflect this, showing the diameter of the wet core shrinking with time. Such an effect is, however, not clear in the experimental data, suggesting that an extension to the dry shell approach may be required for this system. One idea is to allow for a 'damp shell', whereby the a certain fraction of the pore-volume in the shell remains filled by the continuous phase. Work on such an extension to the model is currently in progress.
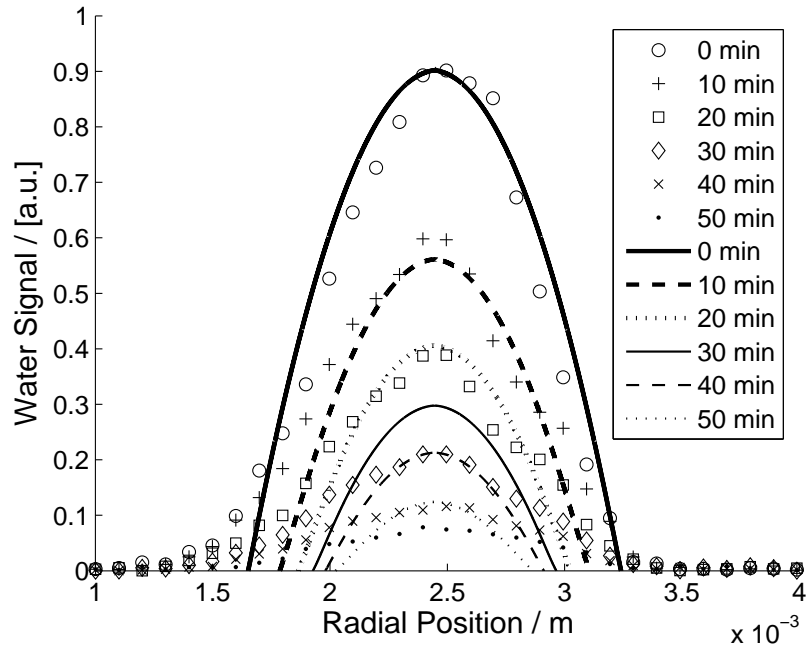
Figure 11: *Simulated moisture profiles in a drying detergent droplet (lines) compared with experimental observations (markers) from Griffith [20]. Measured and simulated profiles are displayed at 10 minute intervals.*

The new droplet drying model gives additional information about the drying droplet. For example, **Figure 12** shows the time evolution of the individual component masses. The mass of solids increases as sodium sulphate crystalises out of solution. This is also reflected in the decreasing solute mass, which tends to a constant value equal to the mass of LAS in the system.

Figure 13 shows the position of the receding dry shell interface as drying proceeds. As demonstrated by (26), the growing dry shell acts as a resistance to further moisture evaporation. In the simulation, the tortuosity of the shell is taken as $\sigma = 10$, which is representative of the values measured by Griffith et al. [21].

Figure 14 shows the solids volume fraction profiles through the drying history. Initially, the crutcher mix droplet is homogeneous with a uniform solids volume fraction of 0.36. As the solid particles are relatively immobile, the surface solids volume fraction quickly reaches 0.65, and shell formation is triggered almost immediately. The rigid shell prevents further shrinkage of the droplet, but the solids volume fraction behind this initial shell is still quite low. The dry shell is therefore predicted to have a loosely packed region immediately behind the external skin. As more water is removed, crystallisation causes the solids volume fraction to rise, as is reflected in later profiles. This in turn causes the packing of the dry shell to increase once more.

At around 40 minutes, all of the sodium sulphate has crystallised out of solution. This corresponds with the removal of all the water from the lye phase. At this point, there is no further mechanism within the model to increase the solids volume fraction and the dried particle is therefore predicted to have a loosely packed centre. In practice, some of the
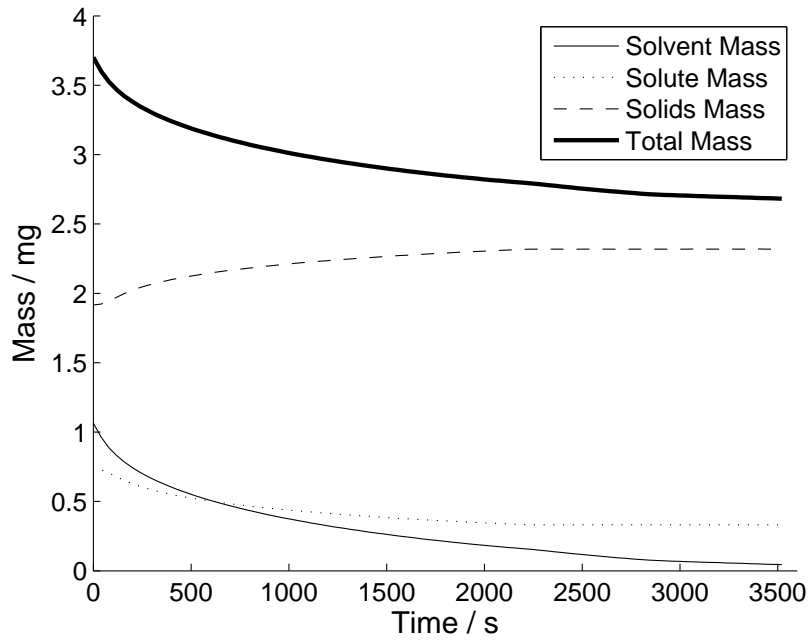
Figure 12: *Simulated evolution of total droplet mass together with the mass of each of the three components in the model droplet.*
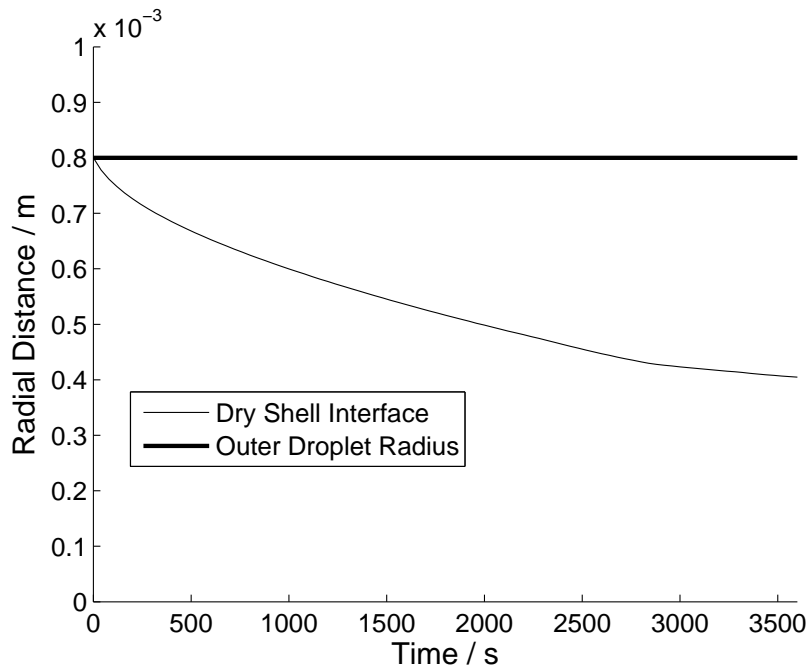
Figure 13: *Simulated time evolution of the dry shell interface during the drying of a droplet of crutcher mix.*

25
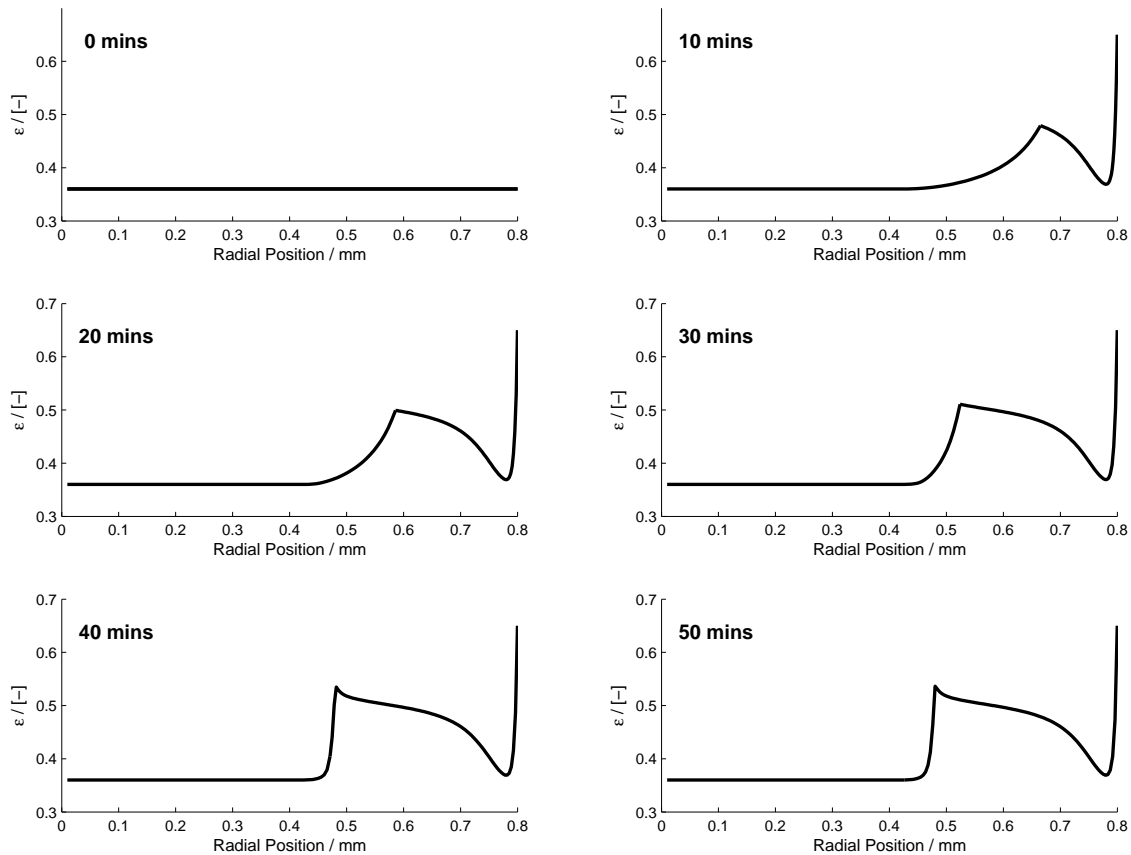
Figure 14: *Simulated solids volume fraction, ε, profiles at 10 minute intervals during the drying of a crutcher mix droplet.*

LAS will solidify as water is removed from the neat phase, but it still seems likely that the centre of the dried particles will be less dense than their outer regions.

Tracking the sodium sulphate mass fraction in the solute, ξ, allows profiles of the concentration of sodium sulphate in the lye phase to be reconstructed. **Figure 15** shows some such profiles plotted at 10 minute intervals through the drying of a crutcher mix droplet. It is seen that the concentration stays relatively constant around 30wt% until around 40 minutes. At this point it falls quickly to zero across the entire droplet. As discussed above, this leads to the cessation of solid crystallisation at the same point in the drying history. The observation of a relatively constant sodium sulphate concentration agrees with experimental results for similar systems. Griffith [20] used ^{23}Na and ^{1}H NMR to observe the drying of a vial of crutcher mix over an extended period. ^{23}Na NMR could track the amount of sodium sulphate in solution as the vial dried. This was found to decrease in step with the free water content, indicating its concentration was approximately constant.
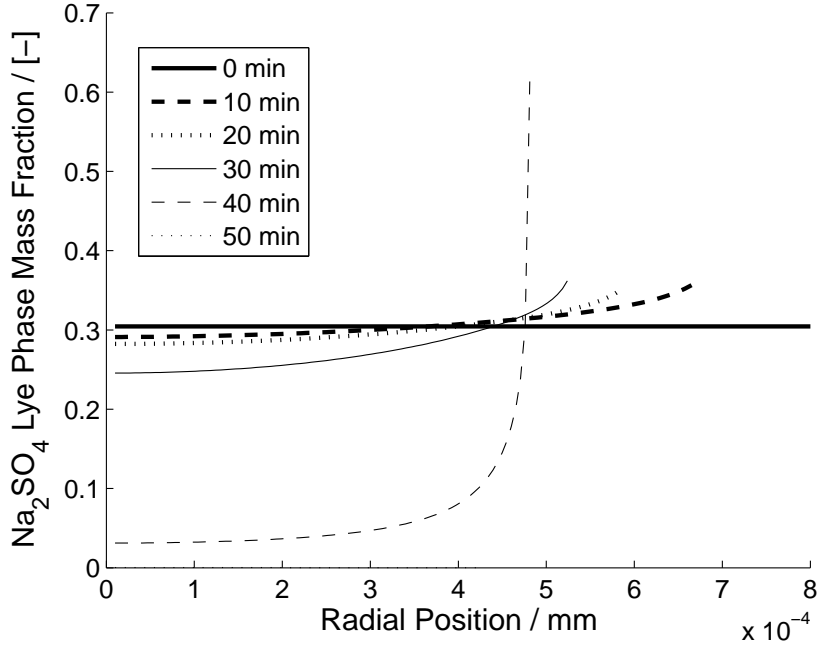
Figure 15: *Simulated lye phase sodium sulphate concentration profiles at 10 minute intervals during the drying of a crutcher mix droplet.*

5.2 Drying a Droplet Containing Colloidal Silica

The second test case simulated is the drying of a colloidal silica droplet containing 16 nm particles suspended in water at an initial mass fraction of 30%. This system was modelled by Handscomb et al. [24] prior to shell formation and compared with experimental results from Nešić and Vodnik [39] at two different drying air temperatures. This comparison demonstrated that the results from the core drying model agreed well with experimental data. After shell formation, this system demonstrates the application of shell thickening and subsequent wet shell drying with bubble formation, as discussed in Sections 3.2 and 3.4 respectively.

To simulate this system using the current model the solute mass fraction is initialised to a very small number, 10^{-9}, thus approximating the pure water continuous phase. Colloidal silica forms a gel at mass fractions above 40%. Nešić and Vodnik [39] report the solids diffusion coefficient in this gel phase as

$$\mathrm{D} = \exp\left(-\frac{28.1 + 282\omega_D}{1 + 15.47\omega_D}\right) , \tag{55}$$

where ω_D is the solids mass fraction. In this example, a size dependent diffusion coefficient is not employed as there is only one particle size throughout. Prior to gel formation, experimental observations suggest that internal convection currents keep the drying droplets well mixed. To simulate this, the diffusion coefficient, (55), is set to 10^{-7} m^{2}s^{-1} – a relatively large value – at low solids concentrations. This gives the functional form for the diffusion coefficient shown in **Figure 16**, where the discontinuity at the point of gel

27
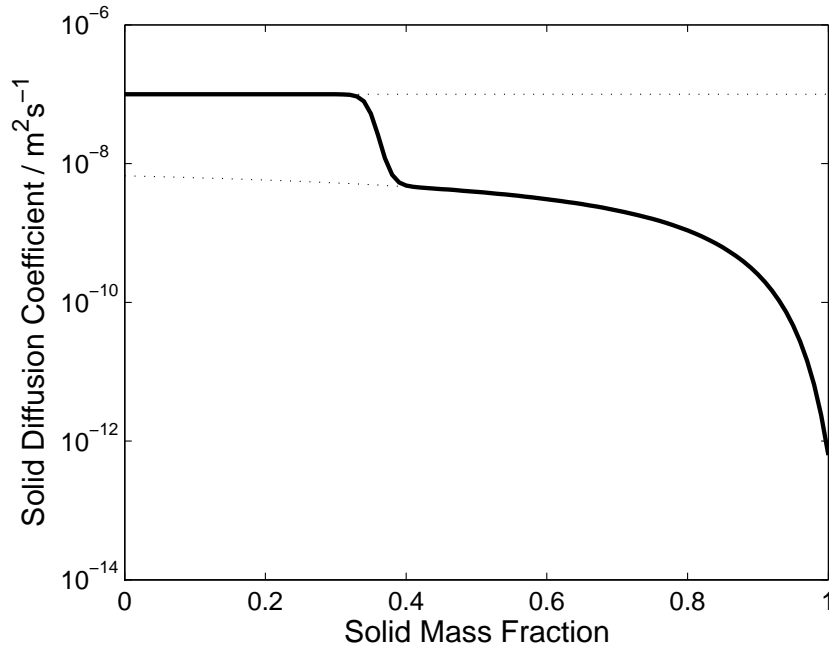
Figure 16: *Plot of the solids diffusion coefficient used to simulate the drying of a colloidal silica droplet.*

formation has been removed through use a hyperbolic tangent blending function similar to (54).

As explained in Section 3.2.1, the Young's Modulus and Poisson's ratio of the colloidal silica shell are required to determine the buckling pressure. Smith et al. [50] measure the shear modulus of wet silica gels, from which the Young's modulus can be calculated, given knowledge of the Poisson's ratio, ν. Using $\nu = 0.2$, as was measured by Scherer [46] for similar silica gels, gives the estimated Young's modulus for the system as 1 MPa. This is relatively low, suggesting that the shell should be expected to buckle repeatedly as the droplet dries leading to considerable thickening. However, the films measured to obtain this figure were composed of 540 nm particles — considerably larger than those in the present system. The sensitivity to this quantity is investigated below.

When the growing bubble meets the internal boundary of the wet shell region, the model switches from the wet to dry shell mode as discussed in Section 3.4.4. The dry shell tortuosity used in (26) is $\sigma = 10$, based on the crust diffusion coefficient reported by Nešić and Vodnik [39]. When the temperature of the droplet reaches $100°$C, the remaining water will boil. Given long enough in the dryer, all the remaining water will be vaporised and the temperature of the dried particle will rise to that of the drying air.

Direct comparisons with the experimental data at $T_{\text{gas}} = 101°$C and $T_{\text{gas}} = 178°$C are presented in **Figure 17 (a)** and **(b)** respectively. A shell was deemed to have formed once the solids volume fraction at the surface of the droplet exceeded 0.58, at which point the shell thickening regime commenced. This figure is chosen by assuming a random packing of the mono-sized particles, [54].

28

At both temperatures, the agreement between the predicted droplet mass and that measured experimentally is very good. For the droplet drying in air at $101°$C, the droplet temperature prediction is initially good, but the model under-predicts the rate of the temperature rise following shell formation. This could be due the assumption of a uniform droplet temperature. It is also not clear whether the reported data relates the the temperature at the centre or surface of the droplet.

Figure 17 (b) shows the results for a colloidal silica droplet drying in air at $178°$C. As the air temperature is above the boiling point of water, it is expected that this droplet will undergo boiling. This is immediately clear from the figure. The switch to dry shell drying, (§3.4.4), occurs at $t = 31.6$ s, at which point the droplet temperature begins to rise rapidly. At $t = 36.0$ s, when the temperature reaches $178°$C — the boiling point of water — the boiling regime is said to commence, (§3.3.2). The remaining water in the droplet is removed by boiling, during which time the temperature remains constant. Once all the moisture has been removed, at $t = 42.8$ s, the droplet mass ceases to decrease and the temperature rises to that of the drying air. The prediction of the droplet temperature for this example are seen to be in very good agreement with the experimentally observed values.

Figure 18 shows the evolution of the particle structure for the droplet drying with $T_\text{gas} = 178°$C. The different drying regimes are clearly visible and it is possible to see the morphology of the droplet at a given time in the drying history. Thickening commences at $t = 23.2$ s, after which the wet shell thickens considerably until the pressure required to cause continued buckling is greater than the pressure drop across the shell. For the droplet with $T_\text{gas} = 178°$C, this critical pressure is 9.6 MPa. The small relative pore size in a shell of 16 nm particles means the surface menisci can support a large pressure drop, (12). Rapid evaporation resulting from drying in air at $178°$C also favours the formation of a thicker crust, (17). The pressure predicted across the shell at the end of thickening is broadly inline with maximum stresses in silica films measured by Guo and Lewis [23].

The shell stops thickening at $t = 31.4$ s, at which point there is a brief period of wet shell drying lasting only 0.2 s. During this period the central vapour bubble grows until it meets the inner shell surface. In this example, the radius of the bubble when it meets the shell is $b = 0.2R$, which is relatively small.

As discussed above, dry shell drying commences at $t = 31.6$ s, with the switch to the boiling regime at $t = 36.0$ s. Both these points are clearly identified in Figure 18, where the different dry shell growth rates in the dry shell and boiling regimes is also visible.

Figure 19 shows the simulated evolution of the solids volume fraction within the droplet of colloidal silica, drying with $T_\text{gas} = 178°$C. Profiles are plotted at 5 s intervals. The profile shown in bold is that at $t = 23$ s when the solids volume fraction at the surface reaches 0.58 and the shell forms. After this, the droplet continues to shrink whilst the shell thickens. The solids volume fraction in this shell region is 0.58 whilst the fraction in the core region is considerably less. This is clear from the two profiles shown in the thickening regime. Close examination of these curves also shows that the solids volume fraction in the core immediately adjacent to the thickening shell is slightly less than that a short distance further in. This is because the growing shell boundary is modelled as a solids
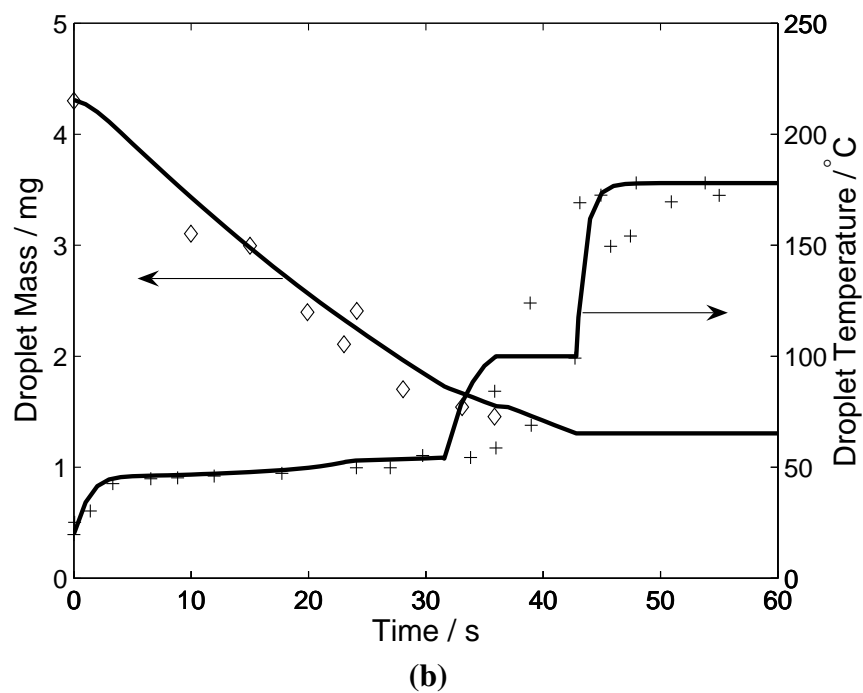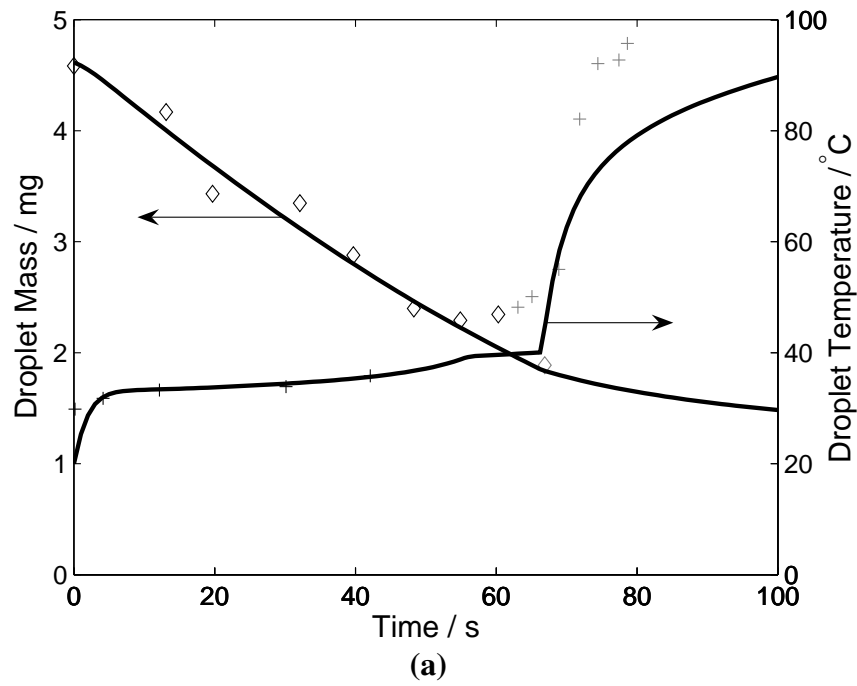
Figure 17: *Simulated drying of a colloidal silica droplet (lines) compared with experimental results from Nešić and Vodnik [39] (points) at: (a) $T_{\text{gas}} = 101°C$ and $R_0 = 0.972$ mm; and (b) $T_{\text{gas}} = 178°C$ and $R_0 = 0.95$ mm.*

30
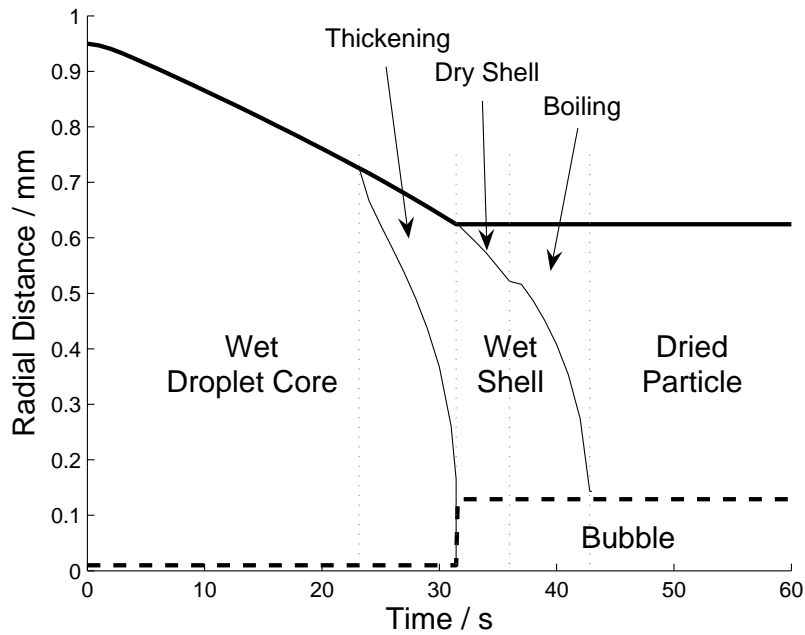
Figure 18: *Plot illustrating the predicted morphological evolution of a droplet of colloidal silica drying in air at* $178°C$.

sink, as discussed in Section 3.4.2. At the end of drying, the solids profile is predicted to be uniform across the particle and is shown by the bold dashed line in Figure 19.

The Young's modulus of the shell used to produce the figures in this section was $E = 1$ MPa. However, as mentioned above, the films measured by Smith et al. [50] to obtain this figure were composed of 540 nm particles — considerably larger than the 16 nm particles suspended in the droplets simulated here. The sensitivity of the results to the choice of E was therefore studied. The droplet mass and temperature profiles were found to be relatively insensitive to the choice of Young's modulus, with the timing of the wet shell to dry shell switch varying by less than 1 s as E was varied over three orders of magnitude. However, as is clear from **Figure 20**, the magnitude of the Young's modulus is of fundamental importance in determining the dimensions of the final dried particle. Droplets which form shells with a larger E produce larger particles with narrower shells, as might be expected. The figure also shows that higher peak pressures are found in droplets forming weaker shells. This is because the such shells continue to deform, leading to thicker shells capable of supporting a larger pressure drop.

6 Conclusion

This paper extended the droplet drying model introduced by Handscomb et al. [24] and focussed on the simulation of droplets drying in the presence of a outer shell. The new model allows for a period of shell thickening wherein the droplet can continue to shrink after a surface shell has formed. The point at which thickening ceases is discussed with
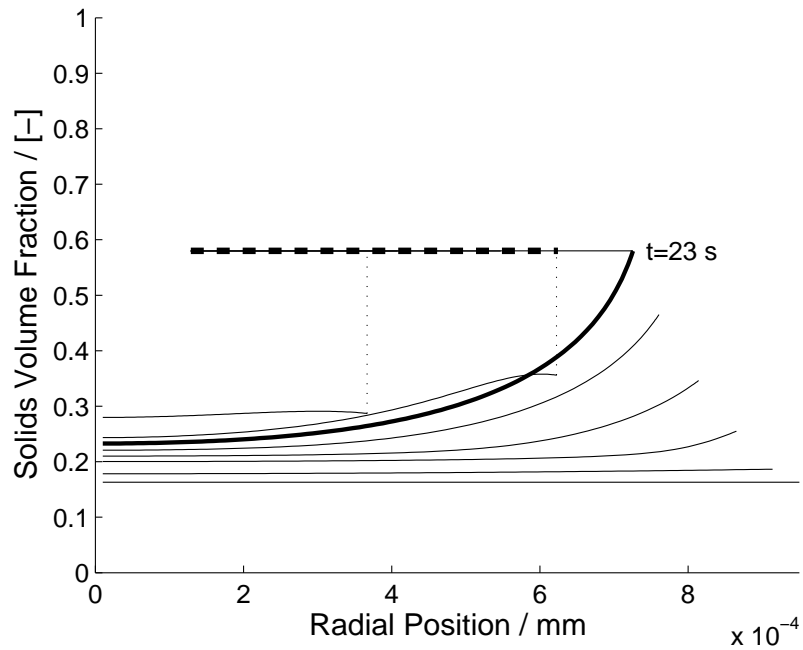
Figure 19: *Simulated solids volume fraction profiles during the drying of a colloidal silica droplet in air at $T_{\text{gas}} = 178°C$. Profiles plotted at 5 s intervals, with the $t = 23$ s profile at the point of shell formation highlighted in bold. The final dried particle solids profile in shown dashed in bold.*
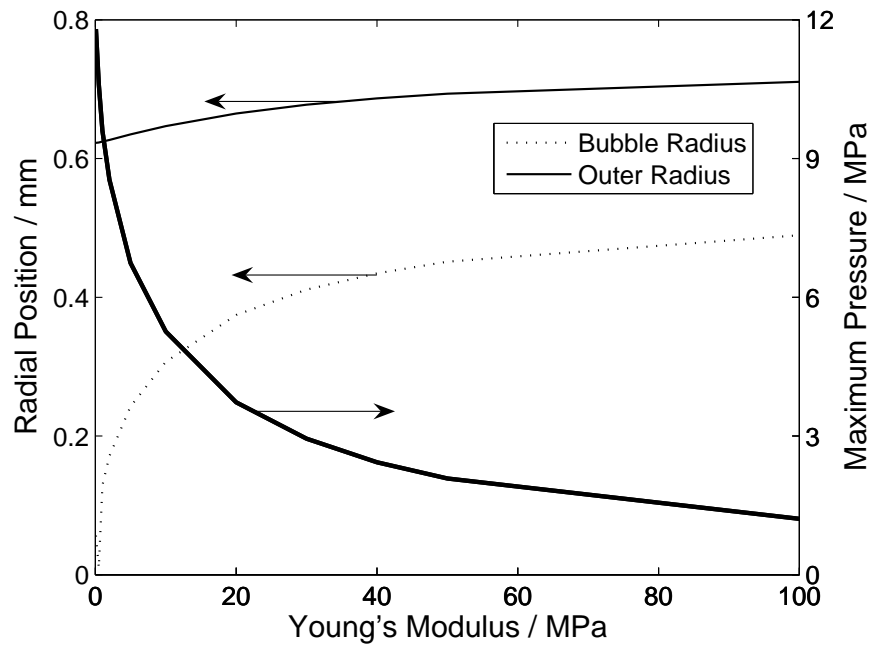
Figure 20: *Plot showing how the Young's modulus of the shell affects the final particle size, shell thickness and maximum stress in the droplet, i.e., the pressure at the end of shell thickening.*

reference to the structural properties of the growing shell.

Once a rigid crust has formed, two drying models were introduced, termed the wet and dry shell approaches. In the wet shell approach, the solids remain wetted by the continuous phase throughout and a gas bubble grows in the centre of the particle. This drying route enables the prediction of hollow dried particles. The dry shell model uses the idea of a receding interface separating a wet core from a moisture-free crust region. Droplets that dry purely through this route will be solid, but the dry shell equations may also be used for droplets drying through the wet shell route once the growing bubble and shell meet. The physical considerations behind both of these models are considered and their implementation within the present droplet drying framework is presented.

Two systems have been simulated with the aim of demonstrating the new capabilities of the model introduced in this paper. The simulation of a crutcher mix droplet shows that, whilst the present model is clearly a simplification of the real physical system, it is nevertheless capable of capturing some key features of interest. The agreement with experimental measurements from the literature is good and the new model gives additional insight into some of these observations. The model also gives predictions about the expected morphology of the dried particles. The simulation of a droplet of colloidal silica in water demonstrates all the post-shell formation features of the new model. Again, the agreement with experimental data is shown to be good and hollow particles are predicted.

The new drying model introduced by Handscomb et al. [24] and extended in this paper can be used to simulate a wide range of different droplet drying systems. The model yields a wealth of information — solute profiles, moments of the solid particle number density, droplet temperature and size — and, furthermore, is capable of predicting a wider range of dried particle morphologies than any previous description.

Nomenclature

Greek Characters

Λ_B	Dimensionless ratio of solvent and solute densities	[-]
γ	Surface tension	[N·m^{-1}]
ε	Solids volume fraction	[-]
κ	Permeability	[m^2]
μ	Viscosity	[Pa·s]
ν	Poisson's ratio	[-]
ξ	Fraction of sodium sulphate in the solute	[-]
ρ	Bulk density	[kg·m^{-3}]
ρ^0	Material density	[kg·m^{-3}]
σ	Tortuosity	[-]
ω	Mass fraction	[-]

Operators

$\overline{B}^{(j)}$ Superficial volume average of B associated with phase j

$\langle B \rangle^{(j)}$ Intrinsic volume average of B associated with phase j

Roman Characters

B_m	Spalding mass transfer number	[-]
C	Molar concentration	[kmol·m^{-3}]
D	Solids diffusion coefficient	[m^2 s^{-1}]
$\mathcal{D}_{\text{eff}}$	Effective diffusion coefficient	[m^2 s^{-1}]
$\bar{D}_{\text{A,air}}$	Diffusion coefficient of water vapour in the drying gas	[m^2 s^{-1}]
E	Young's modulus	[Pa]
G	Linear growth rate	[m·s^{-1}]
$\mathcal{H}_R$	Relative humidity	[-]
ΔH^{vap}	Latent heat of vaporisation	[J·kmol^{-1}K^{-1}]
L	Internal coordinate - particle diameter	[m]
L_{min}	Minimum stable crystal size	[m]
$\dot{N}_0$	Particle nucleation rate per unit volume	[# m^{-3} s^{-1}]
N	Number density function	[# m^{-4}]
P	Pressure	[Pa]
Q	Heat penetrating into the droplet	[J·s^{-1}]
R	Radius of the drying droplet	[m]
R	Gas constant	[J·kmol^{-1}K^{-1}]
S	Radius of the inner edge of the shell	[m]
Sh*	Modified Sherwood number	[-]
T	Shell thickness	[m]
T_d	Droplet temperature	[K]
V	Volume	[m^3]
b	Radius of the central bubble	[m]
k	Boltzmann constant	[J·K^{-1}]
k_{sink}	Sink diffusion coefficient	[m·s^{-1}]
m_a	a^{th} integer moment of the internal coordinate	[m^{a-3}]
$\dot{m}''$	Mass vapour flux from the droplet	[kg·m^{-2}s^{-1}]
$\dot{m}_{\text{vap}}$	Total rate of solvent evaporation	[kg·s^{-1}]
$\boldsymbol{n}$	Mass flux with respect to a stationary reference frame	[kg·m^{-2}s^{-1}]
n_r	Radial mass flux	[kg·m^{-2}s^{-1}]
p	Partial presure	[Pa]
r	Internal coordinate - radial position	[m]
r''	Volume average interfacial production rate	[kg·m^{-2}s^{-1}]
r_M	Radius of curvature	[m]
t	Time	[s]

u	Dry-mass basis moisture fraction	[-]
v_r	Radial velocity	[m·s^{-1}]
z	Non-dimensionalised spatial coordinate	[-]

Superscripts and Subscripts

$^+$	The inner edge of the outer coordinate system
$^-$	The outer edge of the inner coordinate system
A	Solvent
B	Solute
D	Solids
L	Left-hand end of the domain
R	Right-hand end of the domain
buck	Buckling conditions
c	Continuous phase
crit	Critical conditions
d	Discrete phase
eqm	equilibrium conditions
gas	Bulk drying gas conditions
sat	saturated conditions

Abbreviations

LAS	Linear Alkylbenzene Sulfonate
NMR	Nuclear Magnetic Resonance

A Summary of Model Equations and Boundary Conditions

This appendix gives the complete model formulation. The equations are presented in the form in which they are solved, *i.e.,* following the coordinate transformation discussed in Section 4. For each drying regime, the number of spatial domains considered is stated, followed by the equations solved in each. The boundary conditions are then listed and, finally, the ordinary differential equations describing the evolution of the spatial domains are given.

A.1 Prior to Shell Formation

Before the formation of a shell, there is one coordinate system spanning the entire physical domain, $[b, R]$. This domain is mapped onto the interval $[0, 1]$ through application of the transform discussed in Section 4.

The continuous phase equation to be solved is

$$\frac{\partial}{\partial t} \left[(1 - \varepsilon) \rho^{(c)} \langle \omega_B \rangle^{(c)} \right]$$

$$+ \frac{1}{(r_\mathrm{R} - r_\mathrm{L}) \left[r_\mathrm{L} + z (r_\mathrm{R} - r_\mathrm{L}) \right]^2}$$

$$\times \frac{\partial}{\partial z} \left[\left[r_\mathrm{L} + z (r_\mathrm{R} - r_\mathrm{L}) \right]^2 \rho^{(c)} \left((1 - \varepsilon) v_r^{(c)} \langle \omega_B \rangle^{(c)} - \frac{\mathcal{D}_\mathrm{eff}}{r_\mathrm{R} - r_\mathrm{L}} \frac{\partial}{\partial z} \left[(1 - \varepsilon) \langle \omega_B \rangle^{(c)} \right] \right) \right]$$

$$- \frac{1}{r_\mathrm{R} - r_\mathrm{L}} \left[\frac{dr_\mathrm{L}}{dt} + z \left(\frac{dr_\mathrm{R}}{dt} - \frac{dr_\mathrm{L}}{dt} \right) \right] \frac{\partial}{\partial z} \left[(1 - \varepsilon) \rho^{(c)} \langle \omega_B \rangle^{(c)} \right] + \rho_D^0 \frac{\partial \varepsilon}{\partial t} = 0 \; . \tag{A.1}$$

where, $r_\mathrm{L} = b$ and $r_\mathrm{R} = R$. The mass-averaged continuous phase velocity is given by

$$v_r^{(c)} = \frac{\mathcal{D}_\mathrm{eff}}{r_\mathrm{R} - r_\mathrm{L}} \left(\frac{1}{\Lambda_B + \langle \omega_B \rangle^{(c)}} \frac{\partial \langle \omega_B \rangle^{(c)}}{\partial z} - \frac{1}{1 - \varepsilon} \frac{\partial \varepsilon}{\partial z} \right) \; , \tag{A.2}$$

where Λ_B is a dimensionless ratio of material densities,

$$\Lambda_B = \frac{\rho_B^0}{\rho_A^0 - \rho_B^0} \; , \tag{A.3}$$

and the continuous phase density, $\rho^{(c)}$, is

$$\rho^{(c)} = \frac{\rho_A^0 \Lambda_B}{\langle \omega_B \rangle^{(c)} + \Lambda_B} \; . \tag{A.4}$$

The equations for the moments of the solids particle number density are

$$\frac{\partial m_a}{\partial t} = L_\mathrm{min}^a \dot{N}_0 + aG m_{a-1}$$

$$+ \frac{1}{(r_\mathrm{R} - r_\mathrm{L}) \left[r_\mathrm{L} + z (r_\mathrm{R} - r_\mathrm{L}) \right]^2} \frac{\partial}{\partial z} \left(\frac{\left[r_\mathrm{L} + z (r_\mathrm{R} - r_\mathrm{L}) \right]^2}{r_\mathrm{R} - r_\mathrm{L}} \mathrm{D} \frac{\partial m_a}{\partial z} \right) \tag{A.5}$$

$$+ \frac{1}{r_\mathrm{R} - r_\mathrm{L}} \left[\frac{dr_\mathrm{L}}{dt} + z \left(\frac{dr_\mathrm{R}}{dt} - \frac{dr_\mathrm{L}}{dt} \right) \right] \frac{\partial m_a}{\partial z} \; , \quad a \in \{0, 1, 2\}$$

and the solids volume fraction, ε, is given by

$$\frac{\partial \varepsilon}{\partial t} = \frac{\pi}{6} L_\mathrm{min}^3 \dot{N}_0 + \frac{\pi}{2} G m_2$$

$$+ \frac{1}{(r_\mathrm{R} - r_\mathrm{L}) \left[r_\mathrm{L} + z (r_\mathrm{R} - r_\mathrm{L}) \right]^2} \frac{\partial}{\partial z} \left(\frac{\left[r_\mathrm{L} + z (r_\mathrm{R} - r_\mathrm{L}) \right]^2}{r_\mathrm{R} - r_\mathrm{L}} \mathrm{D} \frac{\partial \varepsilon}{\partial z} \right) \tag{A.6}$$

$$+ \frac{1}{r_\mathrm{R} - r_\mathrm{L}} \left[\frac{dr_\mathrm{L}}{dt} + z \left(\frac{dr_\mathrm{R}}{dt} - \frac{dr_\mathrm{L}}{dt} \right) \right] \frac{\partial \varepsilon}{\partial z} \; .$$

Zero gradient boundary conditions are applied to all variables at $z = 0$. At $z = 1$, the continuous phase boundary condition is

$$\frac{\partial \langle \omega_B \rangle^{(c)}}{\partial z}\bigg|_{z=1} = (r_R - r_L) \frac{\langle \omega_B \rangle^{(c)} \dot{m}''}{\rho^{(c)} \mathcal{D}_{\text{eff}}} \;, \tag{A.7}$$

and those for the moments and solids volume fraction are

$$\frac{\partial m_a}{\partial z}\bigg|_{z=1} = -(r_R - r_L) \frac{\dot{m}''}{D \rho_A^0} m_a \;, \qquad a \in \{0, 1, 2\} \tag{A.8}$$

$$\text{and} \quad \frac{\partial \varepsilon}{\partial z}\bigg|_{z=1} = -(r_R - r_L) \frac{\dot{m}''}{D \rho_A^0} \varepsilon \;. \tag{A.9}$$

The extent of the domain changes according to

$$\frac{db}{dt} = 0 \;, \tag{A.10}$$

$$\text{and} \quad \frac{dR}{dt} = -\frac{\dot{m}''}{\rho_A^0} \;, \tag{A.11}$$

where it is assumed that there is no bubble growth prior to shell formation.

A.2 Thickening Regime

In the thickening regime, the physical domain is divided into two regions such that $[r_L, r_R] = [b, S]$ for the internal coordinate system and $[r_L, r_R] = [S, R]$ for the shell region. Both of these domains are mapped onto the interval $[0, 1]$ when the equations are transformed into the z coordinate system, (§4). The solute mass fraction, solids volume fraction and moments in the shell region are denoted $\langle \omega_B \rangle^{(c)}_{\text{shell}}$, $\varepsilon_{\text{shell}}$ and $m_{a,\text{shell}}$ respectively. Having made the appropriate substitutions for the shell region variables, Equation (A.1) is applied unaltered in both regions. Equations (A.5) and (A.6) are unaltered in the core, but in the shell the appropriate equations are now

$$\frac{\partial m_{a,\text{shell}}}{\partial t} = aG m_{a-1,\text{shell}} + \frac{R^2}{(r_R - r_L)\left[r_L + z\left(r_R - r_L\right)\right]^2} \frac{dR}{dt} \frac{\partial m_{a,\text{shell}}}{\partial z}$$
$$+ \frac{1}{r_R - r_L}\left[\frac{dr_L}{dt} + z\left(\frac{dr_R}{dt} - \frac{dr_L}{dt}\right)\right]\frac{\partial m_{a,\text{shell}}}{\partial z}\;, \qquad a \in \{0, 1, 2\} \tag{A.12}$$

and

$$\frac{\partial \varepsilon_{\text{shell}}}{\partial t} = \frac{\pi}{2}G m_{2,\text{shell}} + \frac{R^2}{(r_R - r_L)\left[r_L + z\left(r_R - r_L\right)\right]^2} \frac{dR}{dt} \frac{\partial \varepsilon_{\text{shell}}}{\partial z}$$
$$+ \frac{1}{r_R - r_L}\left[\frac{dr_L}{dt} + z\left(\frac{dr_R}{dt} - \frac{dr_L}{dt}\right)\right]\frac{\partial \varepsilon_{\text{shell}}}{\partial z}\;. \tag{A.13}$$

The boundary conditions at the centre of the droplet are, again, those of zero gradient for all the variables. For the *internal* coordinate system, the boundary conditions at $z = 1$ are

$$
\left.\frac{\partial\langle\omega_B\rangle^{(c)}}{\partial z}\right|_{z=1} = \frac{\mathcal{D}_{\text{eff}}^+}{\mathcal{D}_{\text{eff}}^-}\left(\frac{1 - \varepsilon_{\text{shell}}|_{z=0}}{1 - \varepsilon}\right)\left.\frac{\partial\langle\omega_B\rangle_{\text{shell}}^{(c)}}{\partial z}\right|_{z=0}
$$
$$
- (r_{\text{R}} - r_{\text{L}})\frac{\rho_A^0\langle\omega_B\rangle^{(c)}}{\mathcal{D}_{\text{eff}}^-\rho^{(c)}}\left(\frac{\varepsilon - \varepsilon_{\text{shell}}|_{z=0}}{1 - \varepsilon}\right)\frac{dS}{dt} .
$$
(A.14)

for the continuous phase, where $\mathcal{D}_{\text{eff}}^+$ and $\mathcal{D}_{\text{eff}}^-$ represent the effective diffusion coefficient for the continuous phase calculated at S^+ and S^- respectively. The boundary conditions on the continuous phase equation *in the shell region* are

$$
\left.\langle\omega_B\rangle_{\text{shell}}^{(c)}\right|_{z=0} = \left.\langle\omega_B\rangle^{(c)}\right|_{z=1}
$$
(A.15)

at $z = 0$ and

$$
\left.\frac{\partial\langle\omega_B\rangle_{\text{shell}}^{(c)}}{\partial z}\right|_{z=1} = (r_{\text{R}} - r_{\text{L}})\frac{\langle\omega_B\rangle_{\text{shell}}^{(c)}\dot{m}''}{\rho^{(c)}\mathcal{D}_{\text{eff}}} ,
$$
(A.16)

at the external droplet boundary.

The discrete phase boundary conditions for the inner region at $z = 1$ are

$$
\left.\frac{\partial m_a}{\partial z}\right|_{z=1} = -\frac{1}{r_{\text{R}} - r_{\text{L}}}\frac{k_{\text{sink}}m_a}{\text{D}} , \qquad a \in \{0, 1, 2\} ,
$$
(A.17)

for the moments, and

$$
\left.\frac{\partial\varepsilon}{\partial z}\right|_{z=1} = -\frac{1}{r_{\text{R}} - r_{\text{L}}}\frac{k_{\text{sink}}\varepsilon}{\text{D}} ,
$$
(A.18)

for the solid volume fraction. Zero gradient boundary conditions are applied at both ends of the domain for the discrete phase equations in the shell region.

The bubble, shell and external interfaces evolve according to the equations

$$
\frac{db}{dt} = 0 ,
$$
(A.19)

$$
\frac{dS}{dt} = \left(\frac{\varepsilon_{\text{shell}}|_{z=0}}{\varepsilon_{\text{shell}}|_{z=0} - \varepsilon|_{z=1}}\right)\left(\frac{R}{S}\right)^2\frac{dR}{dt} , \qquad \varepsilon_{\text{shell}}|_{z=0} \neq \varepsilon|_{z=1} ,
$$
(A.20)

$$
\text{and} \quad \frac{dR}{dt} = -\frac{\dot{m}''}{\rho_A^0} .
$$
(A.21)

A.3 Wet Shell Regime

In the wet shell regime, there are again two coordinate systems representing the core and shell regions. Variables in the shell region are notated in the way described in the previous section. Having made the appropriate substitutions for the shell region variables,

Equation (A.1) can be applied in both regions, with the mass-averaged radial velocity given by

$$v_r^{(c)} = \frac{\mathcal{D}_{\text{eff}}}{r_{\text{R}} - r_{\text{L}}} \left(\frac{1}{\Lambda_B + \langle \omega_B \rangle^{(c)}} \frac{\partial \langle \omega_B \rangle^{(c)}}{\partial r} - \frac{1}{1 - \varepsilon} \frac{\partial \varepsilon}{\partial r} \right) + \frac{b^2}{r^2} \frac{db}{dt} . \tag{A.22}$$

In the inner region, the moment equations read

$$
\begin{aligned}
\frac{\partial m_a}{\partial t} =& L_{\text{min}}^a \dot{N}_0 + aGm_{a-1} \\
&+ \frac{1}{(r_{\text{R}} - r_{\text{L}}) \left[r_{\text{L}} + z (r_{\text{R}} - r_{\text{L}}) \right]^2} \frac{\partial}{\partial z} \left(\frac{\left[r_{\text{L}} + z (r_{\text{R}} - r_{\text{L}}) \right]^2}{r_{\text{R}} - r_{\text{L}}} \mathbf{D} \frac{\partial m_a}{\partial z} \right) \\
&- \frac{b^2}{(r_{\text{R}} - r_{\text{L}}) \left[r_{\text{L}} + z (r_{\text{R}} - r_{\text{L}}) \right]^2} \frac{db}{dt} \frac{\partial m_{a,\text{shell}}}{\partial z} \\
&+ \frac{1}{r_{\text{R}} - r_{\text{L}}} \left[\frac{dr_{\text{L}}}{dt} + z \left(\frac{dr_{\text{R}}}{dt} - \frac{dr_{\text{L}}}{dt} \right) \right] \frac{\partial m_a}{\partial z} , \qquad a \in \{0, 1, 2\}
\end{aligned} \tag{A.23}
$$

and the solids volume fraction, ε, is given by

$$
\begin{aligned}
\frac{\partial \varepsilon}{\partial t} =& \frac{\pi}{6} L_{\text{min}}^3 \dot{N}_0 + \frac{\pi}{2} Gm_2 \\
&+ \frac{1}{(r_{\text{R}} - r_{\text{L}}) \left[r_{\text{L}} + z (r_{\text{R}} - r_{\text{L}}) \right]^2} \frac{\partial}{\partial z} \left(\frac{\left[r_{\text{L}} + z (r_{\text{R}} - r_{\text{L}}) \right]^2}{r_{\text{R}} - r_{\text{L}}} \mathbf{D} \frac{\partial \varepsilon}{\partial z} \right) \\
&- \frac{b^2}{(r_{\text{R}} - r_{\text{L}}) \left[r_{\text{L}} + z (r_{\text{R}} - r_{\text{L}}) \right]^2} \frac{db}{dt} \frac{\partial \varepsilon_{\text{shell}}}{\partial z} \\
&+ \frac{1}{r_{\text{R}} - r_{\text{L}}} \left[\frac{dr_{\text{L}}}{dt} + z \left(\frac{dr_{\text{R}}}{dt} - \frac{dr_{\text{L}}}{dt} \right) \right] \frac{\partial \varepsilon}{\partial z} .
\end{aligned} \tag{A.24}
$$

In the shell region, the corresponding equations are

$$
\begin{aligned}
\frac{\partial m_{a,\text{shell}}}{\partial t} =& aGm_{a-1,\text{shell}} \\
&+ \frac{1}{r_{\text{R}} - r_{\text{L}}} \left[\frac{dr_{\text{L}}}{dt} + z \left(\frac{dr_{\text{R}}}{dt} - \frac{dr_{\text{L}}}{dt} \right) \right] \frac{\partial m_{a,\text{shell}}}{\partial z} , \qquad a \in \{0, 1, 2\}
\end{aligned} \tag{A.25}
$$

and

$$\frac{\partial \varepsilon_{\text{shell}}}{\partial t} = \frac{\pi}{2} Gm_{2,\text{shell}} + \frac{1}{r_{\text{R}} - r_{\text{L}}} \left[\frac{dr_{\text{L}}}{dt} + z \left(\frac{dr_{\text{R}}}{dt} - \frac{dr_{\text{L}}}{dt} \right) \right] \frac{\partial \varepsilon_{\text{shell}}}{\partial z} . \tag{A.26}$$

Zero gradient conditions are imposed at the bubble interface for all variables in the inner region. At $z = 1$, for the inner region, the continuous phase boundary condition is

$$
\begin{aligned}
\left. \frac{\partial \langle \omega_B \rangle^{(c)}}{\partial z} \right|_{z=1} =& \frac{\mathcal{D}_{\text{eff}}^+}{\mathcal{D}_{\text{eff}}^-} \left(\frac{1 - \varepsilon_{\text{shell}}|_{z=0}}{1 - \varepsilon} \right) \left. \frac{\partial \langle \omega_B \rangle_{\text{shell}}^{(c)}}{\partial z} \right|_{z=0} \\
&- (r_{\text{R}} - r_{\text{L}}) \frac{\rho_A^0 \langle \omega_B \rangle^{(c)}}{\mathcal{D}_{\text{eff}}^- \rho^{(c)}} \left(\frac{\varepsilon - \varepsilon_{\text{shell}}|_{z=0}}{1 - \varepsilon} \right) \left(\frac{dS}{dt} - \frac{b^2}{S^2} \frac{db}{dt} \right) .
\end{aligned} \tag{A.27}
$$

39

The boundary conditions on the continuous phase equation *in the shell region* are given by (A.15) at $z = 0$ and (A.16) at $z = 1$.

The boundary conditions on the moments in the central region at $z = 1$ are

$$\left.\frac{\partial m_a}{\partial z}\right|_{z=1} = -\frac{1}{r_\mathrm{R} - r_\mathrm{L}}\frac{k_\mathrm{sink} m_a}{\mathrm{D}}, \qquad a \in \{0, 1, 2\} , \tag{A.28}$$

and

$$\left.\frac{\partial \varepsilon}{\partial z}\right|_{z=1} = -\frac{1}{r_\mathrm{R} - r_\mathrm{L}}\frac{k_\mathrm{sink} \varepsilon}{\mathrm{D}} , \tag{A.29}$$

for the solid volume fraction. For the shell region, the boundary conditions for the moments at $z = 0$ are

$$\left.m_{a,\mathrm{shell}}\right|_{z=0} = \left.m_a\right|_{z=1}\left[1 - \left(\frac{b^2}{S^2}\frac{db}{dt} + k_\mathrm{sink}\right)\left(\frac{dS}{dt}\right)^{-1}\right], \qquad a \in \{0, 1, 2\} , \tag{A.30}$$

and

$$\left.\varepsilon_\mathrm{shell}\right|_{z=0} = \varepsilon_\mathrm{crit} . \tag{A.31}$$

for the solids volume fraction. Zero gradient boundary conditions are applied to all the moments at the outer boundary.

The bubble, shell and external interfaces evolve according to the equations

$$\frac{db}{dt} = \frac{R^2}{b^2}\frac{\dot{m}''}{\rho_A^0} , \qquad b > 0 , \tag{A.32}$$

$$\frac{dS}{dt} = \frac{-\left.\varepsilon\right|_{z=1}}{\left.\varepsilon_\mathrm{shell}\right|_{z=0} - \left.\varepsilon\right|_{z=1}}\left(\frac{b^2}{S^2}\frac{db}{dt} + k_\mathrm{sink}\right) , \tag{A.33}$$

$$\text{and} \qquad \frac{dR}{dt} = 0 . \tag{A.34}$$

A.4 Dry Shell Regime

In the dry shell regime, the drying droplet is split into a core and shell region, but spatial evolution equations are only solved in the core region. The spatial domain of interest therefore spans $[b, S]$. The continuous and discrete phase equations in this region are given by (A.1), (A.5) and (A.6). Zero gradient boundary conditions are applied to all variables at both ends of the domain, except for the continuous phase equation at $z = 1$. For this variable, the boundary condition is

$$\left.\frac{\partial \langle \omega_B \rangle^{(c)}}{\partial z}\right|_{z=1} = (r_\mathrm{R} - r_\mathrm{L})\frac{\langle \omega_B \rangle^{(c)}\dot{m}''}{\rho^{(c)}\mathcal{D}_\mathrm{eff}\left(1 - \left.\varepsilon\right|_{z=1}\right)} . \tag{A.35}$$

The bubble and external particle radii do not change in the dry shell region. The position of the internal shell interface is described by

$$\frac{dS}{dt} = -\left(\frac{R}{S}\right)^2\frac{\dot{m}''}{\rho_A^0\left(1 - \left.\varepsilon\right|_S\right)} . \tag{A.36}$$

References

[1] B. Abramzon and W. A. Sirignano. Droplet vaporization model for spray combustion calculations. *International Journal of Heat and Mass Transfer*, 32(9):1605–1618, 1989. doi:10.1016/0017-9310(89)90043-4.

[2] T. O. K. Audu and G. V. Jeffreys. The drying of drops of particulate slurries. *Transactions of the Institution of Chemical Engineers*, 53(3):165–172, 1975.

[3] A. E. Bayly. Crutcher mix sorption experiments. Personal Communication, 2007.

[4] R. B. Bird, W. E. Stewart, and E. N. Lightfoot. *Transport Phenomena*. John Wiley and Sons, 1st edition, 1960.

[5] R. N. Bracewell. Numerical transforms. *Science*, 248(4956):697–704, May 1990. doi:10.1126/science.248.4956.697.

[6] H. J. H. Brouwers. Particle-size distribution and packing fraction of geometric random packings. *Physical Review E*, 74(031309), September 2006. doi:10.1103/PhysRevE.74.031309.

[7] X. Chen and G. Xie. Fingerprints of the drying behaviour of particulate or thin layer food materials established using a reaction engineering model. *Transactions of the Institution of Chemical Engineers Part C: Food and Bioproduct Processing*, 75(C): 213–222, 1997. doi:10.1205/096030897531612.

[8] X. Chen, W. Pirini, and M. Ozilgen. The reaction engineering approach to modelling drying of thin layer of pulped kiwifruit flesh under conditions of small biot numbers. *Chemical Engineering and Processing*, 40(4):311–320, July 2001. doi:10.1016/S0255-2701(01)00108-8.

[9] X. D. Chen and S. X. Q. Lin. The reaction engineering approach to modelling drying of milk droplets. *Proceedings of the 14th International Drying Symposium*, C:1644–1651, August 2004.

[10] H. Cheong, G. Jeffreys, and C. Mumford. A receding interface model for the drying of slurry droplets. *AIChE Journal*, 32(8):1334–1346, August 1986. doi:10.1002/aic.690320811.

[11] J. M. Coulson, J. F. Richardson, J. R. Backhurst, and J. H. Harker. *Coulson and Richardson's Chemical Engineering: Particle Technology and Separation Processes v. 2*. Coulson and Richardson's Chemical Engineering. Butterworth-Heinemann Ltd, 4th edition, 1996.

[12] E. L. Cussler. *Diffusion, Mass Transfer in Fluid Systems*. Cambridge University Press, 2nd edition, 1997.

[13] N. Dalmaz, H. O. Ozbelge, A. N. Eraslan, and Y. Uludag. Heat and mass transfer mechanisms in drying of a suspension droplet: A new computational model. *Drying Technology*, 25(2):391–400, 2007. doi:10.1080/07373930601184569.

[14] W. H. de Groot, L. Adami, and G. F. Moretti. *Manufacture of Modern Detergent Powders*. Herman de Groot Academic Publisher: Wassenaar, 1995.

[15] G. I. Efremov. Drying kinetics derived from diffusion quation with flux-type boundary conditions. *Drying Technology*, 20(1):55–66, January 2002. doi:10.1081/DRT-120001366.

[16] T. Elperin and B. Krasovitov. Evaporation of liquid droplets containing small solid particles. *International Journal of Heat and Mass Transfer*, 38(12):2259–2267, 1995. doi:10.1016/0017-9310(94)00337-U.

[17] A. Erriguible, P. Bernada, F. Couture, and M. A. Roques. Modeling of heat and mass transfer at the boundary between a porous medium and its surroundings. *Drying Technology*, 23(3):455–472, 2005. doi:10.1081/DRT-200054119.

[18] M. R. Etzel, S.-Y. Suen, S. L. Halverson, and S. Budijono. Enzyme inactivation in a droplet forming a bubble during drying. *Journal of Food Engineering*, 27(1):17–34, 1996. doi:10.1016/0260-8774(94)00078-N.

[19] R. Gamero and J. Martínez. Internal mass transfer during isothermal drying of a porous solid containing multicomponent liquid mixtures. *Drying Technology*, 23 (9-11):1939–1951, 2005. doi:10.1080/07373930500210390.

[20] J. D. Griffith. *The Drying and Absorption Properties of Surfactant Granules*. Phd thesis, University of Cambridge, 2008.

[21] J. D. Griffith, A. E. Bayly, and M. L. Johns. Evolving micro-structures in drying detergent pastes quantified using nmr. *Journal of Colloid and Interface Science*, 315 (1):223–229, November 2007. doi:10.1016/j.jcis.2007.06.050.

[22] J. D. Griffith, A. E. Bayly, and M. L. Johns. Magnetic resonance studies of detergent drop drying. *Chemical Engineering Science*, 63(13):3449–3456, 2008. doi:10.1016/j.ces.2008.03.043.

[23] J. J. Guo and J. A. Lewis. Aggregation effects on the compression flow properties and drying behaviour of colloidal silica suspensions. *Journal of the American Ceramic Society*, 82(9):2345–2358, 1999. doi:10.1111/j.1151-2916.1999.tb02090.x.

[24] C. S. Handscomb, M. Kraft, and A. E. Bayly. A new model for the drying of droplets containing suspended solids. *Chemical Engineering Science*, 2008. doi:10.1016/j.ces.2008.04.051.

[25] P. Hansson. *The Sink-Effect in Indoor Materials: Mathematical Modelling and Experimental Studies*. PhD thesis, University of Gävle, 2003.

[26] D. H. Huntington. The influence of the spray drying process on product properties. *Drying Technology*, 22(6):1261–1287, 2004. doi:10.1081/DRT-120038730.

[27] F. P. Incropera and D. P. DeWitt. *Fundamentals of Heat and Mass Transfer*. John Wiley and Sons, 5th edition, 2002.

[28] M. Kadja and G. Bergeles. Modelling of slurry droplet drying. *Applied Thermal Engineering*, 23(7):829–844, May 2003. doi:10.1016/S1359-4311(03)00014-0.

[29] R. Keey. *Drying of Loose and Particulate Matter*. Hemisphere Publishing Corporation, 1st edition, 1992.

[30] R. B. Keey. *Drying Principles and Practice*. Pergamon Press, 2nd edition, 1975.

[31] M. Kohout, Z. Grof, and F. Štěpánek. Pore-scale modelling and tomographic visualisation of drying in granular media. *Journal of Colloid and Interface Science*, 299 (1):342–351, 2006. doi:10.1016/j.jcis.2006.01.074.

[32] T. Langrish and D. Fletcher. Prospects for the modelling and design of spray dryers in the 21st century. *Drying Technology*, 21(2):197–215, 2003. doi:10.1081/DRT-120017743.

[33] T. Langrish and T. Kockel. The assessment of a characteristic drying curve for milk powder for use in computational fluid dynamics modelling. *Chemical Engineering Journal*, 84(1):69–74, 2001. doi:10.1016/S1385-8947(00)00384-3.

[34] A. Lee and C. Law. Gasification and shell characteristics in slurry droplet burning. *Combustion and Flame*, 85(1):77–93, 1991. doi:10.1016/0010-2180(91)90178-E.

[35] K. Masters. *Spray Drying Handbook*. Longman Scientific and Technical, UK, 5th edition, 1992.

[36] H. Masuda, K. Higashitani, and H. Yoshida. *Powder Technology Handbook*. CRC Press, 3rd edition, 2006.

[37] M. Mezhericher, A. Levy, and I. Borde. Theoretical drying model of single droplets containing insoluble or dissolved solids. *Drying Technology*, 25(6):1025–1032, June 2007. doi:10.1080/07373930701394902.

[38] H. Minoshima, K. Matsushima, H. Liang, and K. Shinohara. Basic model of spray drying granulation. *Journal of Chemical Engineering of Japan*, 34(4):472–478, 2001.

[39] S. Nešić and J. Vodnik. Kinetics of droplet evaporation. *Chemical Engineering Science*, 46(2):527–537, 1991. doi:10.1016/0009-2509(91)80013-O.

[40] *NAG Fortran Library Routine Document: D03PFF*. Numerical Algorithms Group.

[41] S. V. Pennington and M. Berzins. New NAG library software for first-order partial differential equations. *ACM Transactions on Mathematical Software*, 20(1):63–69, March 1994. doi:10.1145/174603.155272.

[42] G. O. Porras, F. Couture, and M. Roques. An convection-diffusion model for convection drying of a shrinking media composed of a binary liquid. *Drying Technology*, 25(7-8):1215–1227, August 2007. doi:10.1080/07373930701438600.

[43] D. Rosenblatt, S. B. Marks, and R. L. Pigford. Kinetics of phase transitions in the system sodium sulfate-water. *Industrial and Engineering Chemistry Fundamentals*, 23(2):143–147, May 1984. doi:10.1021/i100014a002.

[44] Y. Sano and R. B. Keey. The drying of a spherical partical containing colloidal material into a hollow sphere. *Chemical Engineering Science*, 37(6):881–889, 1982. doi:10.1016/0009-2509(82)80176-0.

[45] G. W. Scherer. Theory of drying. *Journal of the American Ceramic Society*, 73(1): 3–14, 1990. doi:10.1111/j.1151-2916.1990.tb05082.x.

[46] G. W. Scherer. Bending of gel beams: method for characterizing elastic properties and permeability. *Journal of Non-Crystalline Solids*, 142:18–35, 1992. doi:10.1016/S0022-3093(05)80003-1.

[47] P. Seydel, A. Sengespeick, J. Blömer, and J. Bertling. Experiment and mathematical modeling of solid formation at spray drying. *Chemical Engineering and Technology*, 27(5):505–510, 2004. doi:10.1002/ceat.200403218.

[48] P. Seydel, J. Blömer, and J. Bertling. Modeling particle formation at spray drying using population balances. *Drying Technology*, 24(2):137–146, 2006. doi:10.1080/07373930600558912.

[49] M. A. Silva, P. J. A. M. Kerkhof, and W. J. Coumans. Estimation of effective diffusivity in drying of heterogeneous porous media. *Industrial and Engineering Chemistry Research*, 39(5):1443–1452, 2000. doi:10.1021/ie990563n.

[50] D. M. Smith, G. W. Scherer, and J. M. Anderson. Shrinkage during drying of silica gel. *Journal of Non-Crystalline Solids*, 188(3):191–206, October 1995. doi:10.1016/0022-3093(95)00187-5.

[51] D. B. Spalding. *Convective Mass Transfer*. Edward Arnold, 1st edition, 1963.

[52] M. A. Stanish, G. S. Schajer, and F. Kayihan. A mathematical model of drying for hygroscopic porous media. *AIChE Journal*, 32(8):1301–1311, June 1986. doi:10.1002/aic.690320808.

[53] S. P. Timoshenko. *Theory of Elastic Stability*. McGraw-Hill, 1st edition, 1936.

[54] N. Tsapis, E. Dufresne, S. Sinha, C. Riera, J. Hutchinson, L. Mahadevan, and D. Weitz. Onset of buckling in drying droplets of colloidal suspensions. *Physical Review Letters*, 94(1), January 2005. doi:10.1103/PhysRevLett.94.018302.

[55] D. Walton and C. Mumford. The morphology of spray-dried particles - the effect of process variables upon the morphology of spray-dried particles. *Transactions of the Institute of Chemical Engineers Part A*, 77:442–460, July 1999. doi:10.1205/026387699526296.

[56] D. Walton and C. Mumford. Spray dried products - characterization of particle morphology. *Transactions of the Institute of Chemical Engineers Part A*, 77:21–37, January 1999. doi:10.1205/026387699525846.

[57] S. R. L. Werner, R. L. Edmonds, J. R. Jones, J. E. Bronlund, and A. H. J. Paterson. Single droplet drying: Transition from the effective diffusion model to a modified receding interface model. *Powder Technology*, 179(3):184–189, 2008. doi:10.1016/j.powtec.2007.06.009.

[58] F. E. W. Wetmore and D. J. LeRoy. *Principles of Phase Equilibria*. International Chemical Series. McGraw-Hill, 1st edition, 1951.

[59] S. Whitaker. Simultaneous heat, mass, and momentum transfer in porous media: a theory of drying. *Advances in Heat Transfer*, 13:119–203, 1977.

[60] D. Won, D. M. Sander, C. Y. Shaw, and R. L. Corsi. Validation of the surface sink model for sorptive interactions between vocs and indoor materials. *Atmospheric Environment*, 35(26):4479–4488, September 2001. doi:10.1016/S1352-2310(01)00223-0.